The Astrophysical Journal, 779:61 (22pp), 2013 December 10 doi:10.1088/0004-637X/779/1/61

EXTRAGALACTIC MILLIMETER-WAVE POINT-SOURCE CATALOG, NUMBER COUNTS AND STATISTICS FROM 771 deg^2 OF THE SPT-SZ SURVEY

L. M. Mocanu[1,2], T. M. Crawford[1,2], J. D. Vieira[3], K. A. Aird[4], M. Aravena[5,6], J. E. Austermann[7], B. A. Benson[1,8], M. Béthermin[9], L. E. Bleem[1,10], M. Bothwell[11], J. E. Carlstrom[1,2,8,10,12], C. L. Chang[1,8,12], S. Chapman[13,14], H.-M. Cho[15], A. T. Crites[1,2], T. de Haan[16], M. A. Dobbs[16], W. B. Everett[7], E. M. George[17], N. W. Halverson[7], N. Harrington[17], Y. Hezaveh[16], G. P. Holder[16], W. L. Holzapfel[17], S. Hoover[1,10], J. D. Hrubes[4], R. Keisler[1,10], L. Knox[18], A. T. Lee[17,19], E. M. Leitch[1,2], M. Lueker[3], D. Luong-Van[4], D. P. Marrone[20], J. J. McMahon[21], J. Mehl[1,12], S. S. Meyer[1,2,8,10], J. J. Mohr[22,23,24], T. E. Montroy[25], T. Natoli[1,10], S. Padin[1,2,3], T. Plagge[1,2], C. Pryke[26], A. Rest[27], C. L. Reichardt[17], J. E. Ruhl[25], J. T. Sayre[25], K. K. Schaffer[1,8,28], E. Shirokoff[17], H. G. Spieler[19], J. S. Spilker[20], B. Stalder[29], Z. Staniszewski[25], A. A. Stark[29], K. T. Story[1,10], E. R. Switzer[30], K. Vanderlinde[31,32], and R. Williamson[1,2]

[1] Kavli Institute for Cosmological Physics, University of Chicago, Chicago, IL 60637, USA; lmocanu@uchicago.edu
[2] Department of Astronomy and Astrophysics, University of Chicago, Chicago, IL 60637, USA
[3] California Institute of Technology, Pasadena, CA 91125, USA
[4] University of Chicago, Chicago, IL 60637, USA
[5] European Southern Observatory, Alonso de Córdova 3107, Vitacura Santiago, Chile
[6] Faculty of Engineering, Universidad Diego Portales, Av. Ejército 441, Santiago, Chile
[7] Department of Astrophysical and Planetary Sciences and Department of Physics, University of Colorado, Boulder, CO 80309, USA
[8] Enrico Fermi Institute, University of Chicago, Chicago, IL 60637, USA
[9] Laboratoire AIM-Paris-Saclay, CEA/DSM/Irfu-CNRS-Université Paris Diderot, CEA-Saclay, Orme des Merisiers, F-91191 Gif-sur-Yvette, France
[10] Department of Physics, University of Chicago, Chicago, IL 60637, USA
[11] Cavendish Laboratory, University of Cambridge, 19 J.J. Thomson Avenue, Cambridge CB3 0HE, UK
[12] Argonne National Laboratory, Argonne, IL 60439, USA
[13] Department of Physics and Atmospheric Science, Dalhousie University, Halifax NS B3H 3J5, Canada
[14] Institute of Astronomy, University of Cambridge, Madingley Road, Cambridge CB3 0HA, UK
[15] NIST Quantum Devices Group, Boulder, CO 80305, USA
[16] Department of Physics, McGill University, Montreal, Quebec H3A 2T8, Canada
[17] Department of Physics, University of California, Berkeley, CA 94720, USA
[18] Department of Physics, University of California, Davis, CA 95616, USA
[19] Physics Division, Lawrence Berkeley National Laboratory, Berkeley, CA 94720, USA
[20] Steward Observatory, University of Arizona, 933 North Cherry Avenue, Tucson, AZ 85721, USA
[21] Department of Physics, University of Michigan, Ann Arbor, MI 48109, USA
[22] Department of Physics, Ludwig-Maximilians-Universität, D-81679 München, Germany
[23] Excellence Cluster Universe, D-85748 Garching, Germany
[24] Max-Planck-Institut für extraterrestrische Physik, D-85748 Garching, Germany
[25] Physics Department, Center for Education and Research in Cosmology and Astrophysics, Case Western Reserve University, Cleveland, OH 44106, USA
[26] Department of Physics, University of Minnesota, Minneapolis, MN 55455, USA
[27] Space Telescope Science Institute, 3700 San Martin Dr., Baltimore, MD 21218, USA
[28] Liberal Arts Department, School of the Art Institute of Chicago, Chicago, IL 60603, USA
[29] Harvard-Smithsonian Center for Astrophysics, Cambridge, MA 02138, USA
[30] Canadian Institute for Theoretical Astrophysics, University of Toronto, 60 St. George St., Toronto, Ontario M5S 3H8, Canada
[31] Dunlap Institute for Astronomy & Astrophysics, University of Toronto, 50 St George St, Toronto, Ontario M5S 3H4, Canada
[32] Department of Astronomy & Astrophysics, University of Toronto, 50 St George St, Toronto, Ontario M5S 3H4, Canada

Received 2013 June 12; accepted 2013 October 18; published 2013 November 25

ABSTRACT

We present a point-source catalog from 771 deg^2 of the South Pole Telescope Sunyaev–Zel'dovich survey at 95, 150, and 220 GHz. We detect 1545 sources above 4.5σ significance in at least one band. Based on their relative brightness between survey bands, we classify the sources into two populations, one dominated by synchrotron emission from active galactic nuclei, and one dominated by thermal emission from dust-enshrouded star-forming galaxies. We find 1238 synchrotron and 307 dusty sources. We cross-match all sources against external catalogs and find 189 unidentified synchrotron sources and 189 unidentified dusty sources. The dusty sources without counterparts are good candidates for high-redshift, strongly lensed submillimeter galaxies. We derive number counts for each population from 1 Jy down to roughly 11, 4, and 11 mJy at 95, 150, and 220 GHz. We compare these counts with galaxy population models and find that none of the models we consider for either population provide a good fit to the measured counts in all three bands. The disparities imply that these measurements will be an important input to the next generation of millimeter-wave extragalactic source population models.

Key words: galaxies: high-redshift – submillimeter: galaxies – surveys

Online-only material: color figures, machine-readable table

1. INTRODUCTION

Emission from extragalactic sources produces bright features on small angular scales in the millimeter-wavelength sky. These sources can be divided into two broad populations: sources with flux density that is flat or decreasing with frequency, consistent with synchrotron emission from active galactic nuclei (AGNs), and sources with flux density increasing with frequency, consistent with thermal emission from dust-enshrouded star-forming galaxies (DSFGs). Synchrotron emission is produced by relativistic electrons in active galaxies; DSFGs emit light when photons from hot, young

stars are absorbed by dust grains and reradiated at longer wavelengths.

The synchrotron-dominated population has been explored for decades through long-wavelength radio surveys. Many of these sources are strong emitters down to millimeter wavelengths. A thorough review can be found in De Zotti et al. (2010). This population is generally split into "steep-spectrum" and "flat-spectrum" sources.

In the context of the unified AGN scheme, flat- and steep-spectrum sources are regarded as the same type of intrinsic object (an AGN-powered radio source), only observed at different orientations relative to the jet. When the line of sight is closely aligned with the relativistic jet, the source appears as a flat-spectrum blazar, showing compact, Doppler-boosted emission from the optically thick jet. The flat spectrum is believed to originate from the superposition of different self-absorbed components of the relativistic jets that have different self-absorption frequencies. There are two main categories of blazars: BL Lacs and flat-spectrum radio quasars (FSRQs), distinguished mainly by the fact that FSRQs exhibit strong emission lines. In contrast, when the source is observed side-on, emission originates mainly in the extended, optically thin radio lobes. These sources are classified as steep-spectrum radio galaxies and are mostly associated with radio luminous elliptical and S0 galaxies. Generally, surveys at 5 GHz and higher are dominated by flat-spectrum sources (De Zotti et al. 2010). In particular, FSRQ sources are expected to be the dominant source population at millimeter wavelengths above ∼10 mJy.

In recent surveys, blazars have been observed to exhibit a break in the synchrotron spectrum at frequencies around 100 GHz (Tucci et al. 2011), but with some emission continuing all the way to the THz regime (González-Nuevo et al. 2010; Planck Collaboration et al. 2013a; López-Caniego et al. 2013). This steepening is caused by the transition from optically thick to optically thin emission from the jet due to energy losses of relativistic electrons through radiation (electron cooling). Gigahertz-peaked spectrum (GPS) sources, with spectral peaks in the GHz range due to synchrotron self-absorption, have also been reported (O'Dea 1998). An essential characteristic of radio sources is their variability due to relativistic shocks in the jet; this can lead to biases in the spectral behavior assessed using non-simultaneous observations (González-Nuevo et al. 2010; López-Caniego et al. 2013).

Owing to the recent expansion of millimeter-wave and submillimeter-wave observing capabilities, the dusty-source population is now undergoing extensive characterization (e.g., Lagache et al. 2005). Statistically significant studies of this population began with the detection of the cosmic infrared background (CIB) in 1996 by the Far Infrared Absolute Spectrophotometer on the *Cosmic Background Explorer* satellite (Puget et al. 1996). The CIB is primarily composed of the integrated light from DSFGs. It was found that half of the energy emitted by galaxies over the history of the universe is in the CIB; optical and UV light is absorbed by dust and reradiated in the far-infrared (Dwek & Arendt 1998; Dole et al. 2006). The *Infrared Astronomy Satellite* (*IRAS*) carried out the first all-sky survey in the mid- and far-infrared (e.g., see review by Sanders & Mirabel 1996), detecting about 20,000 extragalactic sources, most of them at low redshift ($z < 0.3$). These sources are now known as luminous and ultraluminous infrared galaxies (LIRGs and ULIRGs). While normal spiral galaxies have luminosities of roughly $10^{10}\ L_{\odot}$ in the far-infrared, ULIRGs have over $10^{12}\ L_{\odot}$ in this band. The total infrared luminosity of the LIRGs and ULIRGs makes up only a small fraction of the local infrared energy output (Soifer & Neugebauer 1991); however, these galaxies dominate the infrared emission at higher redshifts (Le Floc'h et al. 2005).

The Submillimetre Common-User Bolometer Array camera on the 15 m James Clerk Maxwell Telescope at Mauna Kea in Hawaii was used to perform the first blank-field submillimeter survey to mJy depths at 850 μm (Smail et al. 1997; Barger et al. 1998; Hughes et al. 1998), followed soon after by surveys to similar depths with millimeter-wave instruments such as the Max-Planck-Millimeter-Bolometer (Greve et al. 2004) at 1200 μm on the IRAM 30 m and BOLOCAM at 1100 μm (Laurent et al. 2005) on the Caltech Submillimeter Observatory. These surveys revealed a population of luminous, high-redshift DSFGs, commonly referred to as submillimeter galaxies or SMGs, as the bulk of their energy is emitted at submillimeter wavelengths (see review by, e.g., Blain et al. 2002).

Since SMGs were discovered, numerous studies have been undertaken to understand this source population and its properties (e.g., Ivison et al. 2002; Chapman et al. 2005). The spectral energy distribution (SED) of SMGs is well described by a modified blackbody spectrum at a temperature of roughly 30 K (Kovács et al. 2006; Magnelli et al. 2012). They have stellar masses around $10^{11}\ M_{\odot}$ (Hainline et al. 2011; Michałowski et al. 2012) and total infrared luminosities of $10^{13}\ L_{\odot}$ (Kovács et al. 2006). They are copiously forming stars at rates of 100–1000 $M_{\odot}\ \mathrm{yr}^{-1}$ and are most numerous at redshift $z \sim 2.5$ (Chapman et al. 2005; Wardlow et al. 2011; Smolčić et al. 2012), with a high-redshift tail extending out to $z > 6$ (Riechers et al. 2013; Weiß et al. 2013; Vieira et al. 2013). It is generally thought that the majority of bright SMGs originate in mergers (Engel et al. 2010), which cause their high star formation rates; this in turn leads to many supernova explosions and to the production of large quantities of dust (Gall et al. 2011). SMGs are among the largest gravitationally bound objects at their epochs and are precursors to the most massive galaxies (Blain et al. 2004).

A remarkable property of SMGs is that they can be detected from 500 μm to about 2 mm independently of redshift, such that the luminosity is roughly proportional to the flux density for $1 < z < 10$. This is due to the fact that redshift dimming is compensated by observing the galaxy closer to the peak of its SED (negative *K*-correction; Blain 1996). Also, this implies that measurements of the CIB at 220 GHz (1.4 mm) are sensitive to the complete history of emission from DSFGs.

Vieira et al. (2010, hereafter V10) reported the discovery of a population of very bright and rare dust-dominated sources in ∼100 deg^2 of South Pole Telescope (SPT) data. These sources had no counterparts in the *IRAS* catalog, implying that they could not be members of the local U/LIRG population. Consequently, they were hypothesized to be either local galaxies with dust temperatures too cold to be detected by *IRAS* or high-redshift galaxies, either intrinsically ultra-bright or strongly lensed by massive galaxies or clusters along the line of sight—as lensing increases the observed flux density, making the sources appear brighter. Theoretical models had previously predicted such a sample of strongly lensed SMGs (Blain 1996; Negrello et al. 2007).

Subsequent follow-up of those sources confirmed that they are high-redshift, strongly lensed SMGs. The first line of evidence, outlined in Greve et al. (2012), is based on Atacama Pathfinder Experiment 850 μm and 350 μm follow-up on 11 of the brightest lensed candidates. The analysis to determine the photometric redshifts of the sources in a statistical fashion

Table 1
SPT Fields Used in This Work

Name	Season	R.A. (°)	Decl. (°)	ΔR.A. (°)	ΔDecl. (°)	No. Sectors	Effective Area (deg^2)
ra5h30dec-55	2008	82.5	−55.0	15	10	3 × 3	86.7
ra23h30dec-55	2008	352.5	−55.0	15	10	3 × 3	100.5
ra21hdec-60	2009	315.0	−60.0	30	10	6 × 3	153.5
ra3h30dec-60	2009	52.5	−60.0	45	10	8 × 3	232.0
ra21hdec-50	2009	315.0	−50.0	30	10	6 × 3	198.5
Total							771.2

Notes. The locations and sizes of the fields included in this work. For each field we give the center of the field in right ascension (R.A.) and declination (decl.), the extent of the field in R.A. and decl., the number of sectors the field is divided into (see Section 2.4.1), and the effective field area as defined by the apodization mask.

found that these galaxies lie at a median redshift of $z \sim 3.3$, higher than previously identified SMG samples (e.g., Chapman et al. 2005), which, together with their observed flux density, implies very high luminosities. However, compared to the empirical luminosity–temperature relation of the population of unlensed sources, their dust temperatures are characteristic of regular SMGs, arguing that these objects are unlikely to be so intrinsically luminous. This suggests that the objects are strongly lensed members of the normal SMG population. Recently obtained Atacama Large Millimeter/submillimeter Array (ALMA) imaging and spectroscopy (Vieira et al. 2013) of a larger ($N \sim 25$) sample of SPT-discovered sources selected from the catalog presented in this paper demonstrates that they are indeed high-redshift objects—with a measured spectroscopic redshift distribution with a mean of $\bar{z} = 3.5$ (Weiß et al. 2013)—that are strongly lensed by foreground galaxies, with most sources resolved into arcs or Einstein rings (Hezaveh et al. 2013).

The Herschel Multi-tiered Extragalactic Survey (Oliver et al. 2010) and the Herschel Astrophysical Terahertz Large Area Survey (Clements et al. 2010) have also identified a population of very bright dusty sources. A discussion of the detection of lensed SMGs based on *Herschel* data can be found in Negrello et al. (2010) and Wardlow et al. (2013). Millimeter-wave point-source catalogs and number counts have also recently been released by the Atacama Cosmology Telescope (ACT; Marsden et al. 2013) and Planck (Planck Collaboration et al. 2013d).

The SPT has now completed a 2500 deg^2, three-band survey of the millimeter-wave sky. Due to the sensitivity and angular resolution of the SPT, these survey data contains a large number of extragalactic point sources (which are unresolved by the arcminute beam). These sources are of high astrophysical and cosmological interest, relevant for studying the early stages of galaxy formation and their subsequent evolution. The multi-band data allow differentiation between source populations. Apart from their astrophysical importance, emissive sources are also significant contaminants to the small-scale ($\ell \gtrsim 2500$) cosmic microwave background (CMB) power spectrum. Understanding the properties of these source populations is thus essential for CMB analyses, for instance, for separating primary CMB anisotropy power from secondary effects such as lensing and Sunyaev–Zel'dovich (SZ) effects. Measurements of source counts also help constrain the point-source contribution to noise and bias in SZ galaxy cluster surveys.

This is the second point-source catalog paper released from the SPT-SZ survey. The previous point-source analysis, V10, presented a point-source catalog and number counts derived from an 87 deg^2 field surveyed by SPT in 2008, using only two-band data. The spectral index between 150 and 220 GHz was used to classify sources as synchrotron or dust dominated. This analysis improves upon previous results by bringing the total catalogued area to ∼771 deg^2 and extending the analysis to include the 95 GHz band.

This paper is organized as follows. SPT observations and the data reduction procedure are described in Section 2. The mapmaking and source-finding algorithms are also detailed in this section. In Section 3, we present the flux density deboosting procedure used to estimate the intrinsic flux densities and spectral indices of sources and detail their classification as synchrotron dominated or dust dominated. The source catalog and a discussion of extended sources and cross-matching with external catalogs are found in Section 4. Total and by-population source number counts in each observation band are presented in Section 5. In Section 6, we discuss the source populations and compare the number counts to predictions of galaxy evolution models. We present conclusions in Section 7.

2. OBSERVATIONS AND DATA REDUCTION

2.1. Instrument and Survey

The SPT is a 10 m telescope located at the Amundsen-Scott South Pole station in Antarctica (Carlstrom et al. 2011). At 150 GHz (2 mm), the SPT has arcminute angular resolution and a 1 deg^2 diffraction-limited field of view. The SPT was designed for high-sensitivity millimeter/submillimeter observations of faint, low-contrast sources, such as CMB anisotropies. The first survey with the SPT, designated as the SPT-SZ survey, was completed in 2011 November and covers a ∼2500 deg^2 region of the southern extragalactic sky in three frequency bands, 95, 150, and 220 GHz, corresponding to wavelengths of 3.2, 2.0, and 1.4 mm. The fields were surveyed to depths of approximately 40, 18, and 70 μK arcmin at 95, 150, and 220 GHz, respectively.[33]

2.2. Observations

This paper uses data from five fields observed by the SPT in 2008 and 2009. The fields are referred to using the J2000 coordinates of their centers, right ascension (R.A.) in hours and declination (decl.) in degrees. Table 1 lists the positions and effective areas of these fields. These are the same fields used for the CMB power spectrum analysis in Keisler et al. (2011,

[33] Throughout this work, the unit K refers to equivalent fluctuations in the CMB temperature, i.e., the temperature fluctuation of a 2.73 K blackbody that would be required to produce the same power fluctuation. The conversion factor is given by the derivative of the blackbody spectrum (dB_ν/dT), evaluated at 2.73 K.

hereafter K11). The total effective area used for the catalog and analysis in this work is 771 deg^2. We use the previously released catalog exactly as it was analyzed in V10 and add 684 deg^2 of newly analyzed data.

The SPT-SZ camera focal plane was composed of six detector modules, each of which could be configured to observe in a different frequency band. In 2008, when the RA5H30DEC-55 and RA23H30DEC-55 fields were observed, there were three modules operating at 150 GHz, two at 220 GHz, and one at 95 GHz; however, the 2008 95 GHz module did not produce survey-quality data. In 2009, when the RA21HDEC-60, RA3H30DEC-60, and RA21HDEC-50 fields were observed, one of the 220 GHz modules was replaced by a fourth 150 GHz module, and the 95 GHz module was upgraded. As a result, the depth of the fields in the three observing bands is different for the 2008 and 2009 observing seasons. In particular, the part of the catalog in this work that comes from the 2008 fields (RA5H30DEC-55 and RA23H30DEC-55) is derived from deeper 220 GHz data but has no 95 GHz data. As a result, the source selection (and relative contributions of the source populations) differs slightly from the catalog derived from the 2009 fields. However, the 150 GHz depths are similar for the two observing seasons.

SPT observations are performed by sequentially scanning across each field back and forth once at constant elevation, then taking a step up in elevation. One of the 2008 fields, RA23H30DEC-55, and the three fields from 2009, RA21HDEC-60, RA3H30DEC-60, and RA21HDEC-50, were observed using a lead-trail scan strategy, such that each field is divided into two halves in R.A. The lead half is observed first. The trail half is then observed such that, due to the Earth's rotation, both are scanned at the same range of azimuth angle. This allows for removal of potential ground-synchronous signal; however, such a signal was not detected. Therefore, we co-add the lead and trail observations together into a single map. Additionally, about two-thirds of the RA21HDEC-50 observations were performed using elevation scans. In this observing mode, the telescope scanned up and down in elevation (at roughly the same speed as in the azimuth scans) but did not move in azimuth, letting the sky field drift through the field of view.

An observation, defined as a complete set of scans covering the field, takes from 30 minutes to a few hours, depending on the field being observed. The final maps for each field used in this work are made from 400–700 individual and complete observations of the field.

2.3. Data Reduction

The data reduction procedure is described in detail in Schaffer et al. (2011). We summarize the method and the differences from that analysis here and refer the reader to that paper for more details.

2.3.1. Timestream Filtering

Each detector measures the brightness temperature of the sky as a function of time. The time-ordered data (TOD) from well-performing detectors are grouped into scans, keeping only data from the regions observed with constant scan velocity. The TOD are recorded at 100 Hz, then filtered in the Fourier domain. In order to avoid noise aliasing, a 25 Hz low-pass filter is applied to each scan to remove signal on scales smaller than roughly 0.5 arcmin—the Nyquist frequency corresponding to the pixel size of the final maps (0.25 × 0.25 arcmin).

Fluctuations in atmospheric emission due to turbulent water vapor become important on large spatial scales, causing low-frequency noise in the TOD. Additionally, the readout system introduces "$1/f$" noise into the TOD. This low-frequency noise is mitigated by a two-step procedure.

First, a Legendre polynomial (of first order for the azimuth scans and ninth order for the elevation scans) is subtracted from the TOD of each detector. Then, the TODs are high-pass filtered in the Fourier domain with a filter cutoff frequency corresponding to a spatial scale of 45 arcmin in the scan direction.

The atmospheric fluctuation signal is highly correlated between the detectors because the detector beams overlap in the turbulent layers of the atmosphere. For this reason, the average of all well-performing detectors in each module is removed from the TOD at each time step. This acts like an isotropic spatial high-pass filter with an angular scale of about $0\overset{\circ}{.}5$.

The TOD filtering described here has the effect of altering the shape of point sources in the maps. In the absence of filtering, the shape of point sources in the maps would simply be the instrument point-spread function (PSF) or beam. The high-pass filtering causes a ringing pattern around sources in the maps, particularly in the scan direction. Moreover, the effects of filtering are map-position-dependent. Those effects are dealt with as described in Section 2.4.2.

2.3.2. Mapmaking

The next step is going from the TOD to maps of the sky. The pointing model has been described in Schaffer et al. (2011). We approximate the sky as flat across each field and use the oblique Lambert equal-area projection with 0.25 arcmin pixels. This projection preserves distances and areas across the field, such that the beam shape will not be distorted across the map, which is important for finding sources with the CLEAN algorithm (described in Section 2.4.2). However, in this projection, the angle between the scan direction and the map rows varies with map position (see Section 2.4.1).

Single-observation maps are made by averaging all TODs that fall in each pixel by inverse-variance weighting based on the detector power spectral densities (PSDs) between 1 and 3 Hz. Single-observation maps with exceedingly high noise are discarded. All maps that pass the cut are then co-added into a final map for each observing band.

The maps are calibrated as follows. The relative calibrations of the TOD between single observations are determined from measurements of the galactic H II region RCW 38. The absolute calibration is obtained by comparing the SPT power spectrum for each season to the *Wilkinson Microwave Anisotropy Probe* (*WMAP7*; Larson et al. 2011) power spectrum across the multipole range $650 < \ell < 1000$. The uncertainty of this calibration in temperature is estimated to be 1.8%, 1.6%, and 2.4% at 95, 150, and 220 GHz, respectively (Reichardt et al. 2012). These uncertainties are highly correlated because the main sources of error, *WMAP7* bandpower errors and SPT sample variance, are nearly identical between bands. We set this band-to-band correlation factor to one in the uncertainty calculation. As a cross-check, we have performed a similar calculation using the recently released Planck CMB power spectrum (Planck Collaboration et al. 2013c), and the results are consistent.

The absolute pointing is calculated by comparing the locations of the brightest sources in each field to their coordinates in the Australia Telescope 20 GHz (AT20G) Survey catalog (Murphy et al. 2010), which has $1''$ rms positional accuracy. The rms positional uncertainty of the brightest ∼40 sources in each field after applying the pointing correction is roughly $4''$in decl. and $4''$in cross-declination (defined as R.A.· cos(decl.)).

2.4. Source-finding

2.4.1. Matched Filter

We construct a matched filter (Tegmark & de Oliveira-Costa 1998) ψ and apply it to the map in the Fourier domain to enhance the signal-to-noise ratio (S/N) of pointlike objects. The matched filter maximizes sensitivity to beam-sized features by downweighting larger and smaller angular scales where the noise is larger and/or signal is lower:

$$\psi \equiv \frac{\tau^T N^{-1}}{\sqrt{\tau^T N^{-1}\,\tau}}, \quad (1)$$

where τ is the source shape and N is the noise covariance matrix, which contains contributions from non-astrophysical signals (map noise) and the CMB. The precise source shape is determined by the convolution of the beam with the map-domain equivalent of all TOD filtering applied before map-making. Given that the TOD filtering (and thus source shape) is map-position-dependent, we divide each map into 3×3 (for ra23h30dec-55), 6×3 (for ra21hdec-60 and ra21hdec-50), or 8×3 (for ra3h30dec-60) sectors (as listed in Table 1) and evaluate τ and the noise separately for each sector. To check whether these sector sizes are appropriate, we tested the effects of applying the mid-sector transfer function (TF) to sources at one side of the sector, and we found those effects to be subdominant to the beam and calibration error even for the brightest sources, and generally a 1%–2% level effect for most sources.

The first ingredient needed for the filter is the beam shape. The SPT beams are measured using a combination of maps of Venus, Jupiter, and the brightest point sources in the fields. The main lobes are well approximated by Gaussian functions with FWHM of 1.′7, 1.′2, and 1.′0 (at 95, 150, and 220 GHz, respectively). Beam sidelobes are unimportant for the scales relevant to point-source analysis, as they are filtered out.

The source shape is determined by constructing maps of simulated point sources in the following way. First, we place a delta function convolved with the beam at the center of each sector. We "reobserve" this signal using the real pointing information and the same TOD filtering as is applied to the real data. The result is a real-space representation of the source shape for each sector. By transforming this into the Fourier domain, we obtain two-dimensional TFs, representing the relative suppression of signal power due to the PSF and filtering as a function of angular scale along the map x and y directions.

Map noise is composed of instrumental and atmospheric noise and contributions from real astrophysical signal—namely, primary and secondary CMB anisotropies (such as the SZ effect) and point sources below the detection threshold. The instrumental and atmospheric noise components are estimated using a jackknife technique. We take all single-observation maps for each band, multiply half of them by -1, and co-add them (using the same weights used in making the normal co-added map) in order to remove all astrophysical signal. We call those maps "difference maps." This procedure is repeated many times, randomly dividing the single observations in half each time. The Fourier transforms of all difference maps are quadrature averaged to obtain the two-dimensional noise PSD, which is equivalent to the noise covariance. An estimate of primary CMB anisotropy is then added to the noise covariance. For this, we take the standard ΛCDM model CMB power spectrum best fit by *WMAP7* (Larson et al. 2011) and SPT data, as presented in K11. Contributions from secondary anisotropies and sources below the confusion limit are small and can be neglected when constructing the matched filter.

In summary, we use the TFs and noise PSDs to construct the matched filters ψ to apply to each map sector.

2.4.2. CLEAN Procedure

In the filtered maps, sources are located using the CLEAN algorithm (Högbom 1974). This algorithm was developed for producing maps in radio interferometry, where irregular baseline coverage or the finite number of antennae results in finite sampling of the Fourier plane. This incomplete mode sampling leads to a beam exhibiting sidelobes ("dirty beam"), which renders the resulting map difficult to interpret. We have a similar "dirty beam," due in our case to the TOD filtering described in Section 2.3.1.

For each sector, we construct a source template τ' by taking the source shape τ, discussed in the previous section, and convolving it with the matched filter ψ:

$$\tau' = \psi\tau. \quad (2)$$

The CLEAN procedure is implemented as follows:

1. Search for the brightest pixel in the map.
2. Construct a source template at the position of this brightest pixel by rotating the template τ at the center of the sector by the difference in angle between the scan direction at the position of the source and the scan direction at the center of the sector.
3. Subtract the filtered source template τ' multiplied by a loop gain factor at the position of the peak. The loop gain is set to 0.1 to account for imperfect source templates and the presence of extended sources.
4. Look for the brightest pixel in the resulting map and loop through this procedure until no peaks are left above the chosen detection threshold.

We choose to run the source-finder down to a 4.5σ level; this is the significance threshold of the final catalog. We chose this value as the threshold where the V10 catalog was found to be roughly 90% pure. We denote the map that remains after performing all the subtractions as the residual map. All the brightest pixels detected by the algorithm are sorted by intensity and grouped into sources using a brightness-dependent association radius between 30 arcsec and 2 arcmin. The position of each source is taken to be the center of brightness of all pixels associated with the source.

The flux density of each source is determined by taking the value of the brightest pixel corresponding to the source from the filtered map and converting it from CMB fluctuation temperature to units of flux density, namely,

$$S(\mathrm{Jy}) = T_{\mathrm{peak}} \cdot \Delta\Omega_{\mathrm{f}} \cdot 10^{26} \cdot \frac{2k_{\mathrm{B}}}{c^2}\left(\frac{k_{\mathrm{B}}T_{\mathrm{CMB}}}{h}\right)^2 \frac{x^4 e^x}{(e^x-1)^2}, \quad (3)$$

where $x = h\nu/(k_{\mathrm{B}}T_{\mathrm{CMB}})$ and the effective solid angle under the source template $\Delta\Omega_{\mathrm{f}}$ is calculated from

$$\Delta\Omega_{\mathrm{f}} = \left[\int d^2k\ \psi(k_x, k_y)\,\tau(k_x, k_y)\right]^{-1}, \quad (4)$$

where k_x and k_y are the angular wavenumbers associated with the x and y coordinates of the map.

The residual map is visually inspected to check for the effectiveness of the procedure and to identify any extended sources. After visual inspection, we remove a few obviously spurious detections caused by CLEAN residuals near the brightest sources. These are consistent with the beam uncertainty. We also remove detections generated by the sidelobe response to extended sources.

The single-band catalogs are combined based on position offset between bands: sources are considered detected in more than one band if the distance between detections in different bands is less than 30 arcsec. This radius is chosen as a compromise between falsely associating sources that are in fact independent detections and missing true associations due to positional uncertainty. Thirty arcseconds is roughly two times the positional uncertainty for a 4.5σ detection in the band with the widest beam (95 GHz; Ivison et al. 2007). We define the detection band of each source as the band in which the source is detected at the highest S/N. The coordinates recorded in the catalog reflect the position of the source in the detection band. If a source is not detected in a band above the CLEAN cutoff significance, the flux density in that band is taken to be the value of the pixel in the residual map at the location found in the detection band map.

3. FLUX DENSITY DEBOOSTING AND CORRECTED SPECTRAL INDICES

The differential number counts, dN/dS, where N is the number of sources with flux density S, are expected to be a very steep function of flux density, which leads to a positive bias in the measured flux densities. We refer to this effect as flux density boosting. Effectively, it is more likely that a source of measured flux density S is intrinsically dimmer and standing on top of a positive noise fluctuation, rather than brighter and on top of a negative noise fluctuation. This occurs because, although Gaussian noise is equally likely to have a positive or negative contribution to the measured flux density of a given source, there exist many more intrinsically dim sources. This bias is more pronounced for low-S/N detections and is closely related to what is referred to as "Eddington bias" (Teerikorpi 2004). We note, however, that the latter term is generally used in the literature to describe the bias in estimating source counts as a function of brightness, as opposed to the brightness of individual sources.

There will also be a small positive flux density bias due to selecting peaks in the map—or, equivalently, maximizing the signal over x and y (e.g., Austermann et al. 2010)—and a small negative flux density bias when taking the flux density of a source detected in one band from the residual map of a different band (due to positional uncertainty in the detection band). The relation of the apparent source S/N to the true S/N due to maximizing over two parameters is expected to be $\mathrm{S/N_{app}} = \sqrt{(\mathrm{S/N_{true}})^2 + 2}$ (e.g., Vanderlinde et al. 2010), which is a $<5\%$ effect at the 4.5σ threshold of this catalog and negligible at higher significances. The bias due to positional uncertainty is also expected to be very small in this catalog, because the positional uncertainty on $>4.5\sigma$ sources is a small fraction of the beam.

3.1. Motivation for Multi-band Deboosting

Crawford et al. (2010) present a method for estimating the flux density of individual sources from multifrequency survey data, which builds upon the simple Bayesian deboosting approach outlined in, e.g., Coppin et al. (2005). In what follows, we motivate this procedure and summarize its main steps. To correct a single-band flux density measurement, the simplest attempt at a Bayesian approach would be to calculate

$$P(S_{\mathrm{true}}|S_{\mathrm{meas}}) \propto P(S_{\mathrm{meas}}|S_{\mathrm{true}})P(S_{\mathrm{true}}), \quad (5)$$

where $P(S_{\mathrm{true}}|S_{\mathrm{meas}})$ is the posterior probability that the flux density of a source is S_{true} given a measured flux density S_{meas}, $P(S_{\mathrm{meas}}|S_{\mathrm{true}})$ is the likelihood of measuring a flux density S_{meas} given a flux density S_{true} (which in the simplest case is a Gaussian centered at S_{true} with a width related to instrumental and atmospheric noise in the maps), and $P(S_{\mathrm{true}})$ is the prior probability of a source to have an intrinsic flux density S_{true} (which is proportional to the differential number counts dN/dS).

The first issue with applying the standard procedure separately to flux densities measured in three bands is that the flux density priors are correlated between bands and cannot be directly separated into a product of one-dimensional distributions.

The second problem with this approach is that the measured flux density in 1 pixel does not correspond to the flux density of a single source, because fainter sources also contribute to the signal. Instead, it is more appropriate to look for the probability that the brightest source in a pixel has a true flux density S_{max}, given that the total flux density in the pixel was measured to be S_{meas}:

$$P(S_{\mathrm{max}}|S_{\mathrm{meas}}) \propto P(S_{\mathrm{meas}}|S_{\mathrm{max}})P(S_{\mathrm{max}}), \quad (6)$$

where $P(S_{\mathrm{meas}}|S_{\mathrm{max}})$ is the likelihood of measuring a total flux density S_{meas} in a pixel given that the brightest source in the pixel has a flux density S_{max}, and $P(S_{\mathrm{max}})$ is the prior probability that the brightest source in the pixel has flux density S_{max}.

Again, $P(S_{\mathrm{meas}}|S_{\mathrm{max}})$ can be approximated by a Gaussian distribution that includes contributions from both faint sources and noise. This is because a large number of sources below the confusion limit contribute to the flux density in a pixel, and thus the distribution of pixel flux densities approaches a Gaussian, as does the contribution from instrumental and atmospheric noise. The positive and negative tails from bright sources have $\sim 10^{-3}$ lower amplitude than the Gaussian part of the pixel distribution (see V10, Figure 3), and their impact on $P(S_{\mathrm{meas}}|S_{\mathrm{max}})$ can be safely neglected.

The prior $P(S_{\mathrm{max}})$ can be written as the probability that a source of flux density S_{max} exists in the pixel multiplied by the probability that no sources brighter than S_{max} exist in the pixel and is proportional to the differential number counts dN/dS, but with an extra exponential suppression given by the mean number of sources with flux density above S_{max}.

Crawford et al. (2010) developed a method to overcome this limitation and estimate individual source properties for the two-band case. This method was used to correct the source flux densities in V10. Here, we extend this calculation by adding a third band.

3.2. Method for Simultaneous Three-band Deboosting

Let S_{95}, S_{150}, and S_{220} be the flux densities measured for a source in the 95 GHz, 150 GHz, and 220 GHz bands, respectively, and ν_{95}, ν_{150}, and ν_{220} be the effective band centers. For each source, we define two distinct spectral indices, α_{150}^{95} and α_{220}^{150}, as the slope of the assumed power-law behavior of the flux density as a function of frequency between 95–150 GHz and

150–220 GHz, respectively:

$$S_{95} = S_{150}\left(\frac{\nu_{95}}{\nu_{150}}\right)^{\alpha_{150}^{95}}$$
$$S_{220} = S_{150}\left(\frac{\nu_{220}}{\nu_{150}}\right)^{\alpha_{220}^{150}}. \quad (7)$$

The effective band centers depend slightly on the spectral index of the source. We calculate the band centers of the SPT bands by assuming a spectral index of 0, which yields 97.6, 152.9, and 218.1 GHz. This approximation does not significantly affect the source flux densities reported here. We want to obtain a three-dimensional posterior probability density $P(S_{95}^{\rm max}, S_{150}^{\rm max}, S_{220}^{\rm max}|S_{95}^{\rm meas}, S_{150}^{\rm meas}, S_{220}^{\rm meas})$ for the true values of the flux densities of the brightest source in a certain pixel in each band, given the measured flux densities. This can be expressed as

$$P\left(S_{95}^{\rm max}, S_{150}^{\rm max}, S_{220}^{\rm max}|S_{95}^{\rm meas}, S_{150}^{\rm meas}, S_{220}^{\rm meas}\right) \propto P\left(S_{95}^{\rm meas}, S_{150}^{\rm meas}, S_{220}^{\rm meas}|S_{95}^{\rm max}, S_{150}^{\rm max}, S_{220}^{\rm max}\right) \cdot P\left(S_{95}^{\rm max}, S_{150}^{\rm max}, S_{220}^{\rm max}\right). \quad (8)$$

Using a Gaussian likelihood approximation, we first calculate the likelihood $P(S_{95}^{\rm meas}, S_{150}^{\rm meas}, S_{220}^{\rm meas}|S_{95}^{\rm max}, S_{150}^{\rm max}, S_{220}^{\rm max})$ to measure the flux densities $(S_{95}^{\rm meas}, S_{150}^{\rm meas}, S_{220}^{\rm meas})$, given that the true flux densities of the brightest source in the pixel are $(S_{95}^{\rm max}, S_{150}^{\rm max}, S_{220}^{\rm max})$:

$$P(S_{95}^{\rm meas}, S_{150}^{\rm meas}, S_{220}^{\rm meas}|S_{95}^{\rm max}, S_{150}^{\rm max}, S_{220}^{\rm max}) = \frac{\exp\left(-\frac{1}{2}\mathbf{r}^T\mathbf{C}^{-1}\mathbf{r}\right)}{2\pi\sqrt{\det\mathbf{C}}}. \quad (9)$$

Here, $\mathbf{C}$ is the noise covariance between bands. This includes contributions from the rms of the co-added map for each band, beam calibration (both diagonal), and *WMAP* power calibration. Also, $\mathbf{r}$ is a residual vector defined as

$$\mathbf{r} = \left\{S_{95}^{\rm meas} - S_{95}^{\rm max}, S_{150}^{\rm meas} - S_{150}^{\rm max}, S_{220}^{\rm meas} - S_{220}^{\rm max}\right\}. \quad (10)$$

3.3. Choice of Priors

Next, we need a prior on $P(S_{95}^{\rm max}, S_{150}^{\rm max}, S_{220}^{\rm max})$. Because the flux densities in the three bands are correlated, it is easier to construct a prior for the flux density in one band and the two spectral indices of the source, $P(S_{150}^{\rm max}, \alpha_{150}^{95}, \alpha_{220}^{150})$. We employ the simplifying assumption that we can separate this prior as

$$P\left(S_{150}^{\rm max}, \alpha_{150}^{95}, \alpha_{220}^{150}\right) = P(S_{150}^{\rm max})P(\alpha_{150}^{95})P(\alpha_{220}^{150}). \quad (11)$$

For the spectral indices, we use flat priors between −3 and 5. The prior $P(S_{150}^{\rm max})$ is obtained from summing the estimated number counts dN/dS of models of synchrotron and dusty-source populations. For synchrotron sources, we use the De Zotti et al. (2005) prediction at 150 GHz and extrapolate it to the other two bands. For dusty sources, we use the M. Negrello (2010, private communication) predictions at 150 and 220 GHz and extrapolate the Negrello et al. (2007) predictions at 850 μm to the 95 GHz band using a spectral index of 3.1 for SMGs (derived from the Arp 220 SED at a redshift ∼3) and 2.0 for the low-redshift ($z < 0.3$) *IRAS* sources. We have checked that using different number count models as priors does not significantly impact the final results.

In separating the prior this way, we have assumed above that the spectral index priors do not depend on the source flux density and are not correlated. In reality, we know that the spectral indices do depend on flux, because the brightest sources are synchrotron dominated. Also, we do expect the two spectral indices to be correlated for most sources, unless there is a strong spectral break between bands. However, the α priors are broad enough to let these correlations emerge from the data themselves; we choose to stay agnostic about the spectral index distribution and to avoid downweighting potentially different SEDs.

The next step is to convert $P(S_{150}^{\rm max}, \alpha_{150}^{95}, \alpha_{220}^{150})$ into a three-flux density prior,

$$P\left(S_{95}^{\rm max}, S_{150}^{\rm max}, S_{220}^{\rm max}\right) = P\left(S_{150}^{\rm max}, \alpha_{150}^{95}, \alpha_{220}^{150}\right)\left|\frac{d\alpha_{150}^{95}}{dS_{95}^{\rm max}}\frac{d\alpha_{220}^{150}}{dS_{220}^{\rm max}}\right|. \quad (12)$$

We define the "detection band" as the band we apply the number counts prior to; prior information in the other two bands is constructed by combining the number counts prior in the detection band with the spectral index priors.

In the expressions above, 150 GHz is chosen as a detection band. In practice, we perform the deboosting procedure with each band in turn chosen as the detection band by modifying the above calculation accordingly. For the flux densities reported in the source catalog, we use the band with the highest significance detection as the detection band. When we derive number counts in one band, we use that band as the detection band for all contributing sources.

We note that the three-band deboosting procedure accounts for correlations between bands not only in the prior information, but also in the uncertainty estimates. Beam calibration and the absolute calibration to *WMAP* are the main sources of band-to-band correlated uncertainty.

3.4. Posteriors

We marginalize over the parameters in the three-dimensional posteriors $P(S_{95}^{\rm max}, S_{150}^{\rm max}, S_{220}^{\rm max})$ and $P(S_{150}^{\rm max}, \alpha_{150}^{95}, \alpha_{220}^{150})$ to obtain one-dimensional posterior probability densities for the true flux densities $S_{95}^{\rm max}, S_{150}^{\rm max}, S_{220}^{\rm max}$ and for the spectral indices $\alpha_{150}^{95}, \alpha_{220}^{150}$. We take the 16%, 50%, and 84% values of the cumulative posteriors as the best-fit values and equivalent 1σ errors.

We construct two distinct sets of posteriors. The first set, used for deriving the estimated source flux densities in the catalog, includes all sources of error described above (map noise, beam, and absolute calibration). The second set is used for deriving number counts. This set of posteriors does not include the beam and calibration errors, as these two sources of error are common to all the sources in the catalog. We account for those errors by including a common noise realization to all the flux densities in each mock catalog that we construct to obtain statistics; this will be detailed in Section 5.

3.5. Deboosted Flux Densities

Figure 1 presents a scatter plot of the flux densities of each source in different bands, for both the raw (left) and deboosted (right) flux density values. We note that we only consider sources that have three-band data for this part of the analysis. We thus leave out the RA5H30DEC-55 and RA23H30DEC-55 fields here. There are several points to note in this figure.

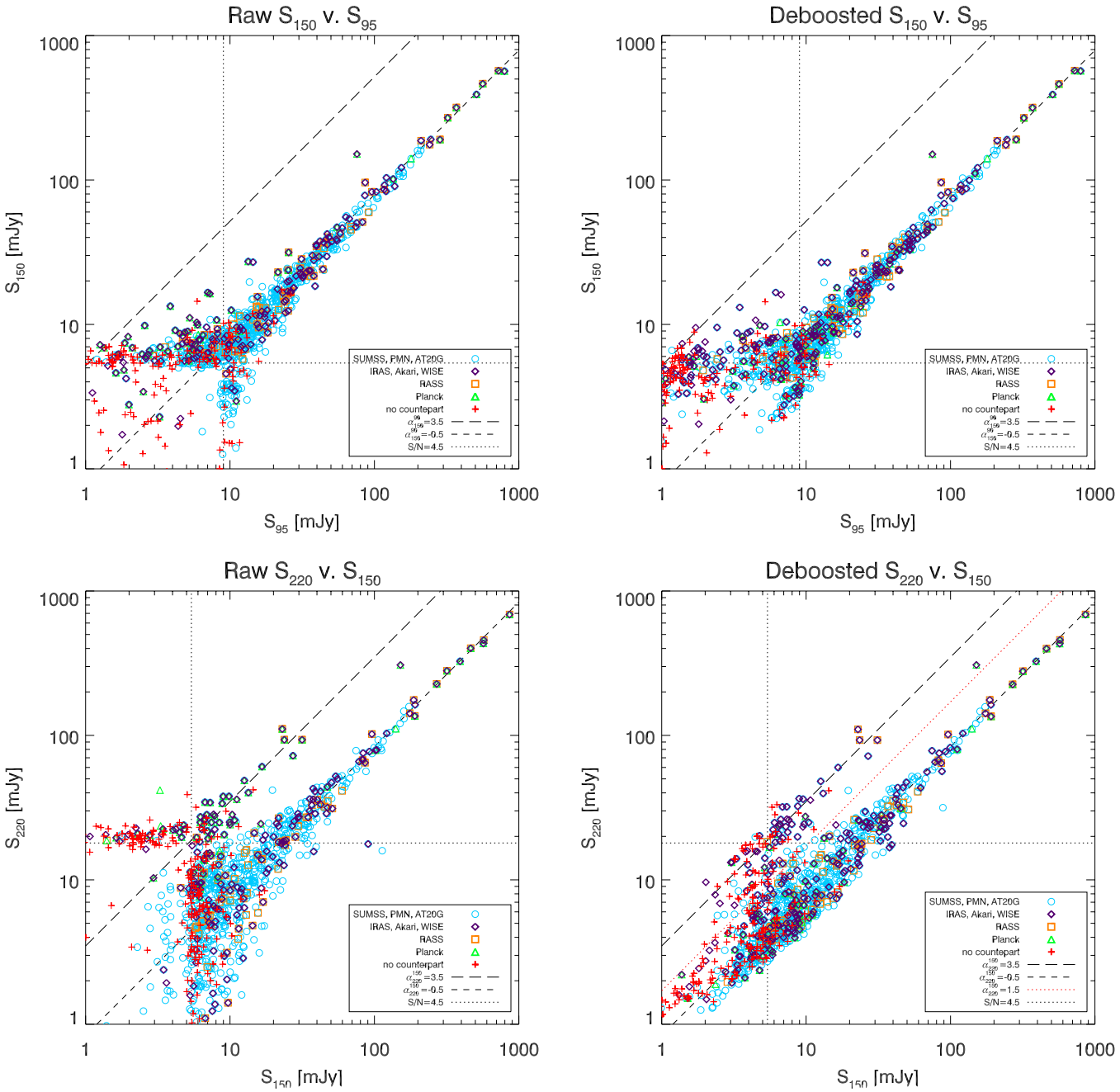

Figure 1. Flux densities in the three bands: 150 GHz flux density vs. 95 GHz flux density, raw (top left) and deboosted (top right), and 220 GHz flux density vs. 150 GHz flux density, raw (bottom left) and deboosted (bottom right) for sources detected above 4.5σ in at least one band. This plot shows the 1128 three-band sources (we leave out the two-band RA5H30DEC-55 and RA23H30DEC-55 fields). The cyan, purple, orange, and green symbols mark SPT-detected sources that have a counterpart in the SUMSS, PMN, AT20G, *IRAS*, *AKARI*, *WISE*, RASS, or Planck catalogs (see Section 4.5 for a description of the external catalogs we cross-match against). The red crosses show SPT sources with no matches in these catalogs. The long-dashed line represents the locus for sources with a spectral index $\alpha = 3.5$, characteristic of dust emission, while the short-dashed line traces $\alpha = -0.5$, typical of synchrotron-dominated sources. The dotted red line represents the $\alpha = 1.5$ threshold for source classification (detailed in Section 3.6). The dotted black line is the 4.5σ detection threshold.

(A color version of this figure is available in the online journal.)

First, from the bottom panels showing the 220 versus 150 GHz flux, one can note that the sources separate into two populations that roughly follow the loci of spectral index −0.5, typical of synchrotron emission, and 3.5, characteristic of dusty galaxies. The top panels, showing 150 GHz versus 95 GHz flux, display many more sources with negative spectral indices, as there are very few sources that are dust dominated down to 95 GHz. This figure only gives a rough picture; the actual source classification is based on an integrated posterior probability density function (PDF) of the spectral index and is described in Section 3.6. Sources that appear below both dotted lines, which are the 4.5σ noise threshold levels, are detected only in the band that is not plotted.

Second, most of the synchrotron sources have counterparts in the SUMSS (or PMN, AT20G) radio catalogs, and roughly half of the dusty sources are in the *IRAS* (or *AKARI*, *WISE*) catalogs (see Section 4.5 for a description of the external catalogs that we cross-match against). While most of the sources without

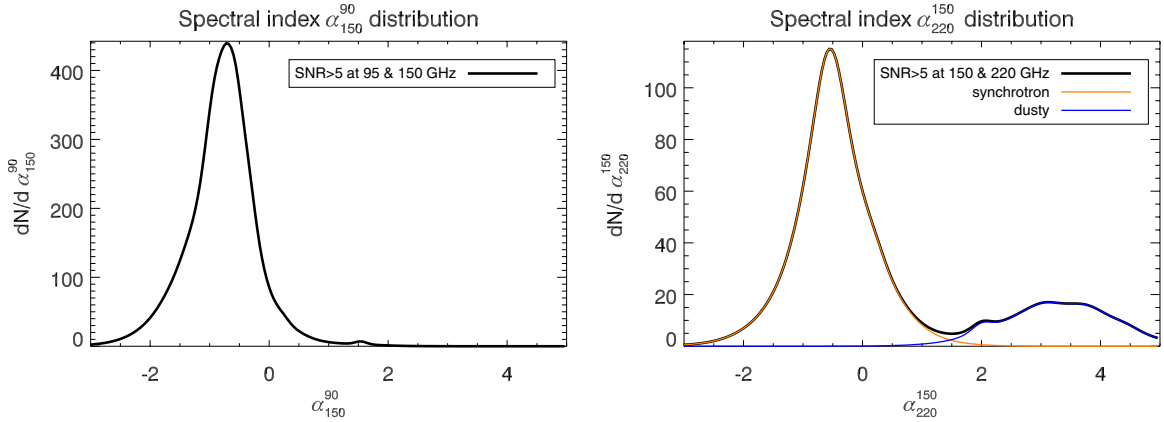

Figure 2. Posterior distribution of spectral indices α_{150}^{95} (left) and α_{220}^{150} (right) for sources detected above 5σ in both adjacent bands that define the respective spectral index. The local minimum of the α_{220}^{150} distribution, α_{220}^{150}=1.5, is chosen as the threshold for source classification. There are 503 sources, 491 synchrotron and 12 dusty, contributing to the α_{150}^{95} distribution. There are 191 sources, 151 synchrotron and 40 dusty, contributing to the α_{220}^{150} distribution.
(A color version of this figure is available in the online journal.)

counterparts are close to the detection threshold, there exist a number of strongly detected objects of both populations that do not have counterparts. This issue will be explored in Section 4.5.

Third, the figure shows the effect deboosting has on the raw flux densities. The lowest S/N sources are the most strongly affected, while strong detections show little change.

3.6. Spectral Indices and Source Classification

We add the spectral index posterior likelihoods for all sources, normalized such that $\int P(\alpha)d\alpha = 1$ for each source, to obtain a distribution of $dN/d\alpha$. Figure 2 shows the distributions of posterior spectral indices α_{150}^{95} and α_{220}^{150} for all sources detected above an S/N of 5 in both adjacent bands that define the spectral index. Again, we only use the three-band data when constructing these plots. The α_{220}^{150} distribution reveals two source populations, with synchrotron sources peaking around a value of -0.5 and dusty sources around 3.5.

We choose the local minimum in the α_{220}^{150} distribution, $\alpha_{220}^{150} = 1.5$, as the threshold for source classification. Sources are classified as synchrotron dominated if there is a less than 50% probability that their posterior α_{220}^{150} is greater than the threshold value, $P(\alpha_{220}^{150} > 1.5) < 0.5$, and as dust dominated if this probability exceeds 50%, $P(\alpha_{220}^{150} > 1.5) \geqslant 0.5$. We choose this classification criterion because, given the 95 GHz map depth, few dusty sources have a well-measured α_{150}^{95}; also, the posterior α_{220}^{150} distribution clearly shows a separation into two populations.

The median spectral index for all 915 three-band synchrotron sources is $\alpha_{220}^{150,\mathrm{sync}} = -0.60$. If we restrict the sample to sources detected above 4.5σ at both 150 and 220 GHz, $\alpha_{220}^{150,\mathrm{sync}} = -0.52$. Applying an additional S/N cut of 5 to the latter criterion, $\alpha_{220}^{150,\mathrm{sync}} = -0.48$. Thus, the brightest synchrotron-dominated sources appear to have slightly flatter spectra. The median spectral index for the dusty sources detected above 5σ at both 150 and 220 GHz is $\alpha_{220}^{150,\mathrm{dust}} = 3.35$.

Figure 3 shows a scatter plot of the two spectral indices, α_{220}^{150} versus α_{150}^{95}, for all 1128 sources with three-band data (we leave out the two-band RA5H30DEC-55 and RA23H30DEC-55 fields). We choose $\alpha_{220}^{150} = 1.5$ (the threshold of synchrotron/dust classification) and $\alpha_{150}^{95} = 0.5$ (by visual inspection of the scatter) as delimiters to split the parameter space into four quadrants. Table 2 lists the distribution of sources falling into each of those four quadrants in several flux density bins.

The two spectral indices show significant correlation, as expected. As listed in Table 2, the majority of sources have both spectral indices of synchrotron type (lower left quadrant), consistent with flux density that is falling with increasing frequency. This fraction increases from about 40% for faint sources ($S_{150} < 6$ mJy) to almost 100% at the bright end. The strongest detected sources are concentrated around the $[-0.5, -0.5]$ point.

The upper right quadrant of Figure 3, encompassing sources with steeply rising flux, is the next most populated. It contains roughly a quarter of the fainter sources ($S_{150} < 6$ mJy), but the fraction drops significantly at bright flux densities.

We also detect sources with high α_{150}^{95} and synchrotron-type α_{220}^{150} (lower right quadrant)—suggesting a peaking or flattening spectrum between 95 and 150 GHz—and sources with low α_{150}^{95} and dust-like α_{220}^{150} (upper left quadrant), consistent with spectra that have a minimum between 95 and 220 GHz. These populations will be discussed in more detail in Section 6.

4. CATALOG DESCRIPTION, STATISTICS, AND EXTERNAL ASSOCIATIONS

We detect 1545 sources above 4.5σ and 1109 above 5σ in any one band. Of these, 1238 above 4.5σ (964 above 5σ), or 80.1% (86.9%), are classified as synchrotron dominated, and 307 (145), or 19.9% (13.1%), are classified as dust dominated.

The map pixel flux density histograms are well approximated by Gaussian distributions, with a positive tail due to emissive sources and a negative tail due to ringing caused by map filtering. The map rms is roughly 2.1 mJy at 95 GHz, 1.2 mJy at 150 GHz, and 3.9 mJy at 220 GHz (see Table 3), with a mild dependence on decl. within a given field (the noise is slightly lower at more negative decl.). We note that the field depths vary slightly as a function of observing time and focal plane configuration for each year.

In the 2009 fields, totaling 584 deg^2 and having three-band data, we detect 640 sources in the 95 GHz map, 915 at 150 GHz, and 344 at 220 GHz. In the two 2008 fields with two-band data, we detect 331 sources at 150 GHz and 191 at 220 GHz. After combining the single-band catalogs, we are left with a total of

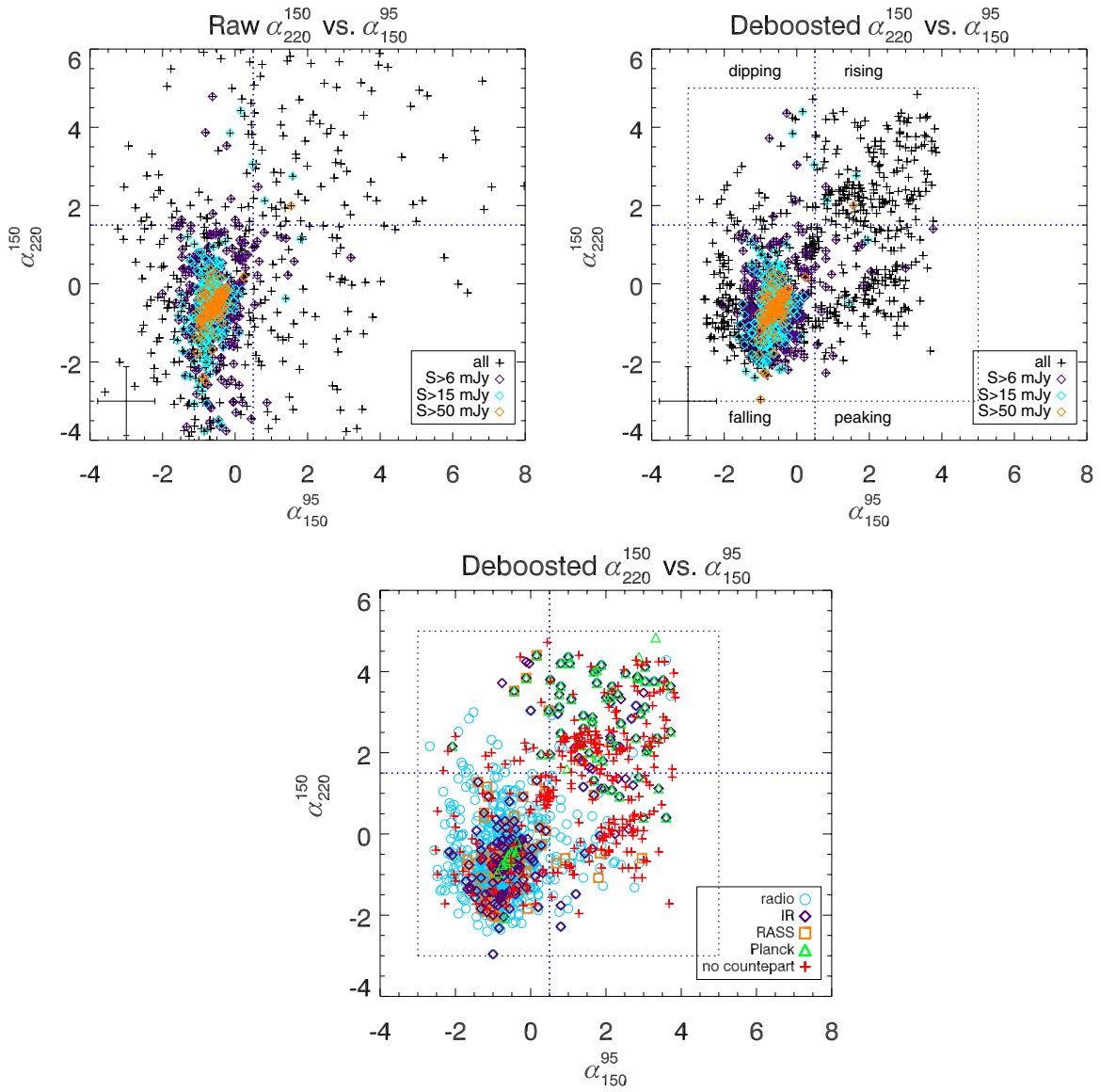

Figure 3. Spectral index α_{220}^{150} vs. α_{150}^{95} for all 1128 sources in the 2009 fields (we leave out the two-band RA5H30DEC-55 and RA23H30DEC-55 fields). The top left panel shows the raw spectral indices, and the top right panel shows the deboosted values. The color coding refers to sources detected above the flux density listed in the legend in at least two bands. The dotted square in the deboosted plot shows the parameter region allowed by the spectral index prior. The dashed blue lines show the threshold α_{150}^{95} and α_{220}^{150} values used as delimiters for the four population quadrants. We note that the actual synchrotron/dusty classification is done probabilistically, based on the posterior PDF, as detailed in Section 3.6. There is a selection effect in that the fraction of sources in each quadrant depends sensitively on the flux threshold of each band. The crosshair on the bottom left shows typical errors for spectral indices of sources near the detection threshold. The bottom panel shows the deboosted values color-coded based on external catalog counterparts of the sources. "Radio" stands for SUMSS, PMN, or AT20G, while "IR" stands for *IRAS*, *AKARI*, or *WISE*. (A color version of this figure is available in the online journal.)

Table 2
Spectral Behavior

Spectral Behavior		All	S_{150} <6 mJy	S_{150} 6–12 mJy	S_{150} 12–36 mJy	S_{150} ⩾36 mJy
Any		1128 (100%)	496 (44.0%)	335 (29.7%)	207 (18.3%)	90 (8.0%)
$\alpha_{150}^{95} < 0.5, \alpha_{220}^{150} < 1.5$	"falling"	753 (66.8%)	206 (41.5%)	262 (78.2%)	196 (94.7%)	89 (98.9%)
$\alpha_{150}^{95} \geqslant 0.5, \alpha_{220}^{150} < 1.5$	"peaking"	162 (14.4%)	131 (26.4%)	29 (8.7%)	2 (1.0%)	0 (0.0%)
$\alpha_{150}^{95} < 0.5, \alpha_{220}^{150} \geqslant 1.5$	"dipping"	41 (3.6%)	28 (5.6%)	10 (3.0%)	3 (1.4%)	0 (0.0%)
$\alpha_{150}^{95} \geqslant 0.5, \alpha_{220}^{150} \geqslant 1.5$	"rising"	172 (15.2%)	131 (26.4%)	34 (10.1%)	6 (2.9%)	1 (1.1%)
$P(\alpha_{220}^{150} \geqslant 1.5) < 0.5$	sync	915 (81.1%)	337 (67.9%)	291 (86.9%)	298 (95.7%)	89 (98.9%)
$P(\alpha_{220}^{150} \geqslant 1.5) > 0.5$	dust	213 (18.9%)	159 (32.1%)	44 (13.1%)	9 (4.3%)	1 (1.1%)

Note. Distribution of spectral behavior for the 1128 sources that have three-band data.

Table 3
Field Depths and Completeness Levels

Name	95 GHz			150 GHz			220 GHz		
	rms (mJy)	50% c. (mJy)	95% c. (mJy)	rms (mJy)	50% c. (mJy)	95% c. (mJy)	rms (mJy)	50% c. (mJy)	95% c. (mJy)
ra5h30dec-55		...		1.27	5.25	8.25	3.35	13.65	21.15
ra23h30dec-55		...		1.24	5.40	7.38	3.56	15.75	21.51
ra21hdec-60	1.95	8.55	11.68	1.13	4.95	6.76	3.94	17.55	23.97
ra3h30dec-60	2.04	8.91	12.17	1.19	5.54	7.57	4.02	17.86	24.40
ra21hdec-50	2.27	9.86	13.46	1.32	5.85	7.99	4.49	19.62	26.79

Note. rms noise and 50% and 95% completeness levels for each field.

Table 4
SPT-SZ 771 deg^2 Point-source Catalog Preview

ID and Coordinates			95 GHz Data		150 GHz Data		220 GHz Data		Spectral Indices and Type					
SPT ID	R.A. (deg)	Decl. (deg)	S/N	$S^{\rm deb}$ (mJy)	S/N	$S^{\rm deb}$ (mJy)	S/N	$S^{\rm deb}$ (mJy)	$\alpha_{95}^{150,\rm deb}$	$\alpha_{150}^{220,\rm deb}$	$P(\alpha_{150}^{220}>1.5)$	Type	Extended	Catalog Assoc.
SPT-S J000038−5347.2	0.161	−53.788	...	...	2.59	$2.73^{+1.47}_{-1.63}$	4.58	$2.60^{+10.62}_{-1.63}$	...	$1.0^{+2.9}_{-2.9}$	0.44	Sync	No	None
SPT-S J000119−5345.1	0.332	−53.752	...	...	1.48	$1.16^{+1.53}_{-0.85}$	4.68	$1.35^{+4.56}_{-0.85}$	...	$1.4^{+2.6}_{-2.8}$	0.47	Sync	No	None
SPT-S J000156−5143.6	0.485	−51.727	...	...	0.00	$0.41^{+0.59}_{-0.26}$	4.57	$0.74^{+0.99}_{-0.43}$	...	$2.2^{+2.0}_{-2.7}$	0.58	Dust	No	None
SPT-S J000212−5927.5	0.553	−59.458	...	...	6.53	$7.45^{+1.31}_{-1.33}$	2.08	$6.13^{+3.06}_{-2.49}$	...	$-0.4^{+1.3}_{-1.5}$	0.02	Sync	No	1
SPT-S J000253−5948.2	0.722	−59.805	...	...	66.12	$80.98^{+3.51}_{-3.51}$	19.63	$69.22^{+7.17}_{-7.17}$	...	$-0.4^{+0.3}_{-0.3}$	0.00	Sync	No	1,2,3
SPT-S J000254−5621.3	0.725	−56.355	...	...	7.41	$9.55^{+1.48}_{-1.48}$	1.19	$5.33^{+2.69}_{-1.57}$	...	$-1.6^{+1.2}_{-0.9}$	0.00	Sync	No	1,2,3
SPT-S J000303−5530.1	0.766	−55.503	...	...	14.37	$19.53^{+1.60}_{-1.60}$	3.15	$11.12^{+3.65}_{-2.94}$	...	$-1.5^{+0.8}_{-0.8}$	0.00	Sync	No	1,2,3
SPT-S J000309−5258.2	0.790	−52.971	...	...	5.92	$7.36^{+1.49}_{-1.52}$	1.33	$4.87^{+2.89}_{-1.78}$	...	$-1.1^{+1.4}_{-1.2}$	0.01	Sync	No	1
SPT-S J000310−5444.9	0.792	−54.749	...	...	25.87	$35.50^{+2.01}_{-2.01}$	8.20	$29.67^{+4.63}_{-4.63}$	...	$-0.5^{+0.4}_{-0.5}$	0.00	Sync	Yes	1,2,3
SPT-S J000313−5905.8	0.805	−59.098	...	...	10.31	$12.37^{+1.33}_{-1.36}$	4.42	$14.66^{+3.85}_{-3.94}$	...	$0.5^{+0.7}_{-0.9}$	0.03	Sync	No	1,2,3

(This table is available in its entirety in a machine-readable form in the online journal. A portion is shown here for guidance regarding its form and content.)

1545 (1109) sources detected above 4.5σ (5σ) in at least one band. Of those, 1128 (816) are from the 2009 data and have three-band information, and 417 (293) are from the 2008 fields and only have two-band information.

4.1. Catalog Description

We construct a catalog with the following entries:

1. Source ID: the IAU designation for the SPT-detected source.
2. R.A.: right ascension (J2000) in degrees.
3. Decl.: declination (J2000) in degrees.
4. S/N_{95}: detection significance (S/N) in the 95 GHz band.
5. $S_{95}^{\rm raw}$: raw flux density (uncorrected for flux density boosting) in the 95 GHz band.
6. $S_{95}^{\rm deb}$: deboosted flux density values encompassing 16%, 50%, and 84% (68% probability enclosed, or 1σ for the equivalent normal distribution) of the cumulative posterior probability density for 95 GHz flux, as estimated using the deboosting procedure described in Section 3.
7. S/N_{150}: detection significance at 150 GHz.
8. $S_{150}^{\rm raw}$: raw flux density at 150 GHz.
9. $S_{150}^{\rm deb}$: deboosted flux density values at 150 GHz.
10. S/N_{220}: detection significance at 220 GHz.
11. $S_{220}^{\rm raw}$: Raw flux density at 220 GHz.
12. $S_{220}^{\rm deb}$: deboosted flux density values at 220 GHz.
13. $\alpha_{150}^{95,\rm raw}$: estimate (from the raw flux density in each band) of the 95–150 GHz spectral index α_{150}^{95}.
14. $\alpha_{150}^{95,\rm deb}$: 16%, 50%, and 84% estimates of the spectral index, based on the posterior probability densities for the spectral index calculated using the deboosting procedure described in Section 3.
15. $\alpha_{220}^{150,\rm raw}$: estimate (from the raw flux density in each band) of the 150–220 GHz spectral index α_{220}^{150}.
16. $\alpha_{220}^{150,\rm deb}$: 16%, 50%, and 84% estimates of the spectral index calculated using the deboosting procedure.
17. $P(\alpha_{220}^{150} > 1.5)$: fraction of the spectral index posterior probability density above the threshold value of 1.5. A higher value of P means the source is more likely to be dust dominated. This is detailed in Section 3.6.
18. Type: source classification (synchrotron or dust dominated), based on whether $P(\alpha_{220}^{150} > 1.5)$ is greater than or less than 0.5.
19. Extended flag: flag for extended sources.
20. External counterparts: external catalogs wherein a source has a match with an offset smaller than the chosen association radius. As described in Section 4.5, we choose an association radius of 1 arcmin for all catalogs except *WISE*, where we use 0.5 arcmin.

The catalog is available for download on the SPT Web site.[34] Table 4 exemplifies the first 10 catalog entries, but a few data columns have been omitted due to space limitations. The catalog association field lists external catalog counterparts for the sources, as described in Section 4.5.

[34] http://pole.uchicago.edu/public/data/mocanu13/

4.2. Completeness

To estimate the completeness of the catalog, we check how well the source-finding algorithm detects a known sample of sources. For this purpose, we take the residual map for each field, which is a good approximation of noise, and add simulated sources of a fixed flux density at random locations. We construct the simulated source profiles from the measured beam convolved with the map-domain equivalent of timestream filtering and matched filter. This is equivalent to the source profile described in Section 2.4.2. We then run the source-finder on those maps to find the number of input sources that are recovered as a function of flux. It follows that the completeness is $f_{\rm compl}(S) = N_{\rm recovered}/N_{\rm input}$. As noise in the maps is Gaussian and uniform to a good approximation, the cumulative completeness is well fit by an error function

$$f_{\rm compl}(S) = \frac{1}{\sqrt{2\pi\sigma^2}} \int_S^\infty e^{-(S'-S_0)^2/2\sigma^2} dS', \qquad (13)$$

where S_0 is the detection threshold. We find the best-fit σ value for each field and band and use this function as an estimate of completeness. The 50% completeness levels are, on average, 9.1 mJy, 5.4 mJy, and 17.6 mJy at 95, 150, and 220 GHz, respectively. We are 95% complete at roughly 12.6, 7.4, and 24.1 mJy at 95, 150, and 220 GHz, respectively. Table 3 shows the depth and the 50% and 95% completeness levels for each field.

We note that we search for both positive and negative sources during the source-finding procedure, such that galaxy clusters with very significant and compact SZ decrements are detected and CLEANed in the maps. We are thus not accounting for any incompleteness caused by sources having their emission canceled by the decrements from these clusters. However, assuming a *WMAP7* cosmology, a Tinker et al. (2008) cluster mass function, and the SPT cluster mass and redshift selection function from Reichardt et al. (2013), we expect roughly one decrement large enough to cancel a 4.5σ point source per 10 deg^2, or roughly 80 in the entire area used here. If there is no spatial correlation between clusters and point sources, then the probability that even one $>4.5\sigma$ point source is being canceled by one of these clusters is very small, roughly 1%. There is, of course, theoretical motivation, as well as some observational evidence, for a correlation between clusters and point sources. But even if every cluster we remove is hiding a 4.5σ source—which is an extremely pessimistic upper limit—this will cause only a few-percent error in the completeness calculation at 95 and 150 GHz. (The 220 GHz completeness calculation is unaffected by SZ.)

4.3. Purity

We estimate purity by running the source-finder on simulated maps. These maps are constructed by taking difference maps that contain only atmospheric and instrumental noise and adding a CMB realization from the best-fit *WMAP7* + K11 CMB power spectrum, estimates of the SZ effect, and Poisson and correlated components of the CIB. We calculate the purity fraction as a function of S/N as $f_{\rm pure} = 1 - N_{\rm false}/N_{\rm total}$, where $N_{\rm false}$ is the number of detections in the simulated maps above a certain S/N, and $N_{\rm total}$ is the total number of sources detected in the real maps above the same threshold. We find the catalog to be 92% pure at 4.5σ in the 150 GHz band.

The simulations used to calculate purity do not include the SZ effect from massive clusters; the SZ effect in the simulations is a Gaussian field with the power spectrum tuned to match the measurement in Shirokoff et al. (2011). Thus, we are not accounting in the purity calculation for possible spurious positive source detections from the wings of very significant (negative) SZ decrements. In practice, such spurious detections are both very rare and easily detectable, so we can remove them from the catalog if necessary. The most significant cluster in these fields is SPT-CL J2106−5844, which is also among the most compact due to its very high redshift ($z = 1.18$; Foley et al. 2011), making it the most likely source of detectable positive wings. This cluster's decrement produces a 5.0σ wing at 150 GHz and a 5.4σ wing at 95 GHz, and we remove these spurious detections from the catalog. The next most significant cluster in these fields is a factor of 1.5 less significant than SPT-CL J2106−5844 (Reichardt et al. 2013), so we do not expect any other clusters to produce detectable positive wings from their SZ decrements.

4.4. Extended Sources

Given the SPT's arcminute resolution, extragalactic sources at redshifts above $z \sim 0.05$ are expected to appear point-like in the maps. Only very nearby sources or AGNs with extended structure (radio lobes or jets) are expected to look extended.

We test all sources detected above an S/N of 5 in any band for extended emission. There are many approaches in the literature to identifying extended objects in photometry data (e.g., Stetson 1987); we choose to fit to a simple extended-source template. We take a cut-out of an unfiltered map around each detected source and fit to it the measured beam convolved with a two-dimensional elliptical Gaussian function, letting the width along two directions and the orientation angle vary. Based on an empirical comparison of $\Delta\chi^2$ for the extended model and visual evidence for extended emission, we chose to flag as extended those sources for which $\Delta\chi^2 > 10$ between the best-fit extended model and the beam-only model.

The flux density calculation uses a source template that consists of a filtered beam. The flux density of an extended object will be underestimated because the effective solid angle under the source template that we use in the flux density calculation (Equation (4)) corresponds to a point source.

We detect 63 extended sources, out of which 37 are synchrotron dominated and 26 are dust dominated. The brightest extended sources are AGNs with extended emission, generally due to lobe structures. This is confirmed by their extended, multiple-blob or jet-like appearance in the corresponding SUMSS image, which we visually inspect for the brightest 20 sources. The brightest dusty extended sources are nearby star-forming galaxies present in the New General Catalogue of Nebulae and Clusters of Stars (NGC). Some examples are NGC 1599, NGC 1672 (Seyfert type 2 nucleus, with strong and extended emission in both radio and infrared), NGC 1566 (the second brightest known Seyfert galaxy, which also appears extended in SUMSS maps), and NGC 7090. Fainter detections include NGC 7083, 7059, 7125 and 7126. All of the extended sources we find have counterparts in external catalogs.

4.5. External Associations

We search several external catalogs for counterparts at the positions of all sources in the catalog. We query the following catalogs:

Table 5
Counterparts in External Catalogs

Name	No. Counterparts	No. Footpr.	Σ (per deg^2)	r_{assoc} (arcmin)	P(random) (%)
SUMSS	1092	22538	29.23	1	2.55
IRAS	98	4349	5.64	1	0.49
RASS	113	2718	3.53	1	0.31
AKARI	82	5583	7.24	1	0.63
Planck	101	587	0.76	1	0.07
WISE	274	54005	70.05	0.5	1.52
PMN	530	1562	2.03	1	0.18
AT20G	277	297	0.39	1	0.03

Notes. Summary of cross-matching with external catalogs. The table lists the catalog name, number of SPT sources with counterparts in that catalog within the listed association radius, the number of sources in that catalog located within the five SPT fields, source density within the SPT fields, chosen association radius, and the probability of random association with an SPT source given the association radius.

1. The Sydney University Molonglo Sky Survey (SUMSS; Mauch et al. 2003) at 36 cm (843 MHz).
2. The Parkes-MIT-NRAO (PMN; Wright et al. 1994) Southern Survey at 4850 MHz.
3. The Australia Telescope 20 GHz Survey (Murphy et al. 2010) at 1.5 cm.
4. The *IRAS* Faint Source Catalog (*IRAS*-FSC; Moshir et al. 1992) at 60 and 100 μm.
5. The *WISE* Source Catalog at 22 μm (W4).
6. The *AKARI*/FIS Bright Source Catalog (Yamamura et al. 2010) at 65, 90, 140, and 160 μm and *AKARI*/IRC Point Source Catalog (Ishihara et al. 2010) at 9 and 18 μm.
7. The Planck Catalog of Compact Sources (PCCS, Planck Collaboration et al. 2013d) at 30, 44, 70, 100, 143, 217, 353, 545, and 857 GHz (1 cm to 350 μm).
8. The ROSAT All-Sky Survey (RASS) Bright Source Catalog (Voges et al. 1999) and Faint Source Catalog (Voges et al. 2000).

These are the most relevant catalogs to search for millimeter-wave selected extragalactic sources in the Southern Hemisphere. SUMSS is the essential radio catalog to check, as it has complete coverage of the SPT fields to a 5σ depth of 6 mJy beam^{-1}. For this reason, we expect most of our significant synchrotron-dominated sources to have counterparts in SUMSS. We add PMN and AT20G in the radio catalog category. The *IRAS* and *AKARI* catalogs are the longest-wavelength infrared catalogs with full-sky coverage and thus the most appropriate catalogs to check for local dust emission from LIRGs and ULIRGs. We also check the *WISE* and Planck catalogs for potential dusty-source counterparts.

We use an association radius of 1 arcmin for all catalogs except *WISE*, for which we use 30 arcsec. These values were chosen based on the positional accuracy of the catalogs and their beam size and by looking at the distribution of offsets between SPT sources and their closest counterpart in each catalog as a function of SPT S/N.

Table 5 shows the number of SPT sources with counterparts in each catalog, the source density, and probability of random association for the chosen radius for each catalog. We note that nearly all of the dusty sources associated with *WISE* or *AKARI* are also in *IRAS*, and nearly all sources found in PMN or AT20G are also found in SUMSS.

Previously unidentified sources are of particular interest. Table 6 lists the number of SPT sources with no counterparts in any of the catalogs listed above, in total and by category, as well as the expected number of false detections (from the simulations used in Section 4.3), given the significance level and total number of detections. The synchrotron/dusty classification is done as described in Section 3.6. We add a subcategory of dusty sources, labeled as "SMGs," which we define to be the sources with $\alpha_{220}^{150} \geqslant 2$ that have no *IRAS* counterparts. This is the subset of sources that Vieira et al. (2013) have demonstrated to have a high probability of being high-redshift, strongly lensed galaxies. We note, however, that the *IRAS* sky coverage is not perfect and there is a possibility that a few low-redshift objects have been missed by the survey.

Table 6
Sources without Counterparts

	S/N (Any Band)			
Category	>4.5	>5	>7	>10
Any	378/244/1545	129/28/1109	20/0/638	6/0/433
Synchrotron	189/195/1238	68/24/964	13/0/599	4/0/419
Dust	189/49/307	61/4/145	7/0/39	2/0/14
SMG	137/36/174	57/4/80	5/0/13	2/0/5

Note. Number of sources without counterparts/expected number of false detections/total sources in each specified category above the listed signal-to-noise level in any one band.

We find that almost 25% (12%) of all sources above 4.5σ (5σ) do not have counterparts, with 15% (7%) of radio sources, 62% (42%) of dusty sources, and 79% (71%) of SMGs lacking external associations. As shown in Table 6, a substantial fraction of sources below 5σ without counterparts—particularly the synchrotron-dominated sources—are likely to be false detections; above 5σ, however, most sources without counterparts in all categories are expected to be real. There are 56 synchrotron sources detected above 5σ at 150 GHz that have no counterparts in external catalogs. This number is rather surprising, given that basically all synchrotron sources above 5σ published in V10 had external associations.

Is it plausible that the SPT could detect synchrotron-dominated sources that were not detected in past radio surveys? Radio sources are known for their variability, so the synchrotron sources without counterparts in radio catalogs might be flaring between the two observation epochs. The SUMSS detection threshold is between 6 and 10 mJy, and the catalog is complete at 18 mJy. A source detected at 5σ at 95 GHz in the SPT survey has a flux density of about 10 mJy. Assuming a spectral index of −0.5, this means that its SUMSS flux density should be around 100 mJy. Therefore, the source could have escaped an SUMSS detection if it flared by a factor of 10 at the time of the SPT

detection, which is a reasonable factor (see, e.g., Aller et al. 2011).

Alternatively, given that some of these sources are only faintly detected at 95 or 220 GHz and their spectral index posteriors are quite wide, it could also be the case that some fraction of them have been misclassified as radio sources. Another possibility is that some faint sources in the SUMSS catalog may have been removed in error by the decision tree used for source selection (according to the SUMSS documentation; Mauch et al. 2003); yet, this is unlikely to have affected more than a few sources.

For any of these explanations, the 7.9 times larger area used in this work makes it more likely to find anomalous sources compared to the V10 analysis. However, even accounting for the area differences, the results show some discrepancy with V10. Considering just the SUMSS catalog, there are 73 synchrotron-dominated sources detected above 5σ at 150 GHz without a counterpart in the four fields analyzed here, and their number in each field is roughly proportional to the area of the field. In retrospect, using just the 2009 results, we would predict 11.3 synchrotron-dominated sources without an SUMSS counterpart above 5σ in the RA23H30DEC-55 field, and 9.8 such sources in the V10 (RA5H30DEC-55) field. In reality, we see seven such sources in the RA23H30DEC-55 field, which is consistent with the prediction, but there is only one such source in the V10 field. Under the assumption of pure Poisson statistics, we would expect one such source or fewer in a field the size of the V10 field less than 0.5% of the time.

We can ask whether there is something particular about the V10 field that would make it less likely to harbor synchrotron-dominated sources with no SUMSS counterparts. The RA23H30DEC-55 field is effectively the same as the V10 field in terms of number of bands and depth, so any difference in the V10 field is not due to having three-band data or less deep 220 GHz data. We have checked that the SUMSS source densities are similar in the five fields. The RA5H30DEC-55 field is at lower galactic latitude than most SPT fields and, as such, has a higher level of diffuse galactic foreground emission. However, diffuse foregrounds are strongly suppressed in the matched filter (which filters out all large-scale emission); furthermore, the RA21HDEC-60 field stretches to as low galactic latitude as the RA5H30DEC-55 field, and the number of synchrotron-dominated sources without counterparts in the RA21HDEC-60 field is typical. We conclude that the discrepancy between the V10 field and the other four fields is likely a statistical fluctuation.

The dusty sources without counterparts are likely high-redshift galaxies, given that nearby objects would be detected by *IRAS*. These are interesting sources to follow up and constitute good candidates for strongly lensed SMGs. Some of the brightest such detections in the survey have already been followed up, as noted in Section 1, and have been found to indeed be strongly lensed.

5. NUMBER COUNTS

We derive source number counts using a bootstrap method outlined in Austermann et al. (2009). For each source in the catalog, we randomly draw 50,000 flux densities from the deboosted three-band flux density posterior, $P(S_{95}, S_{150}, S_{220})$. We thus obtain 50,000 mock source catalogs. We resample each of those mock catalogs by drawing with replacement a number of sources that is a Poisson deviate of the catalog size. For each of the resampled catalogs, we compute the number counts dN/dS in each flux density bin. We correct the counts for completeness in each bin based on the simulations described in Section 4.2. We perform this procedure separately for each field.

We do not explicitly correct for purity, as it is intrinsically accounted for in the Bayesian deboosting as follows. Some sources in the mock catalogs will be assigned sub-threshold flux densities due to drawing from the region of the flux density posterior that is below the detection threshold and will thus be thrown out of the counts.

We combine the number counts from different fields by summing up the counts, weighted by a quantity we denote as "effective area." We define this as the area of the field multiplied by the completeness in each flux density bin. We then use the cumulative distributions of dN/dS over all catalogs to obtain the 16, 50, and 84 percentile points, which represent the median and equivalent 1σ errors on the final counts. Because the fields have varying depths, the lowest few flux density bins only contain contributions from fields with detection thresholds below the bin range. We use all five fields in Table 1 in the number counts. Thus, the 95 GHz counts reflect the three 2009 fields, or 584 deg^2, while the 150 and 220 GHz counts reflect all five fields, totaling 771 deg^2.

We account for sources of uncertainty as follows. Taking Poisson deviates of the real catalog size for the mocks accounts for sample variance. We do not include the uncertainty from variance due to large-scale structure, as the large survey area assures sufficient sampling of structure in the universe. As mentioned in Section 3, because the beam and calibration error are the same for all sources in the catalog, we use a set of flux density posteriors constructed without including the beam and calibration error in the covariance matrix for each source. Rather, we incorporate a realization of beam and calibration noise that is common to all sources in a mock catalog but is different between catalogs. The source flux density posterior includes errors due to map noise and cross-band deboosting. We note that the errors on the number counts are correlated between bins, roughly at the 5% level.

Extended sources contribute less than 8% of the counts in any flux density bin, and typically less than 3%; the effect of their underestimated flux densities is completely subdominant to the statistical errors on the number counts.

We derive number counts for the two source populations using a probabilistic classification method. For each source in the resampled catalogs, which stands as a triplet of flux densities drawn from a posterior, we calculate the spectral index α_{220}^{150} and classify the source as dusty if it exceeds the threshold index. It follows that a source that has $P(\alpha \geqslant 1.5) = p$ will be included in the dusty counts in a fraction p of the resamplings and in the synchrotron counts in the remaining $1 - p$ fraction.

Figure 4 shows source number counts in the three frequency bands. We show the total counts, as well as counts for the synchrotron- and dust-dominated populations. Synchrotron sources are the main component everywhere except for the lowest flux density bins at 220 GHz, where the dust component becomes dominant. The counts are consistent with the results published in V10. Tables 7, 8, and 9 list the number count values in the 95, 150, and 220 GHz bands, respectively.

Figure 5 presents a comparison between our 150 GHz counts, 143 GHz number counts from Planck (Planck Collaboration et al. 2013a), and 148 GHz number counts from ACT (Marsden et al. 2013) (left panel); and our 220 GHz counts, Planck 217 GHz counts, and ACT 218 GHz counts (right panel). The three sets of counts are consistent with one another.

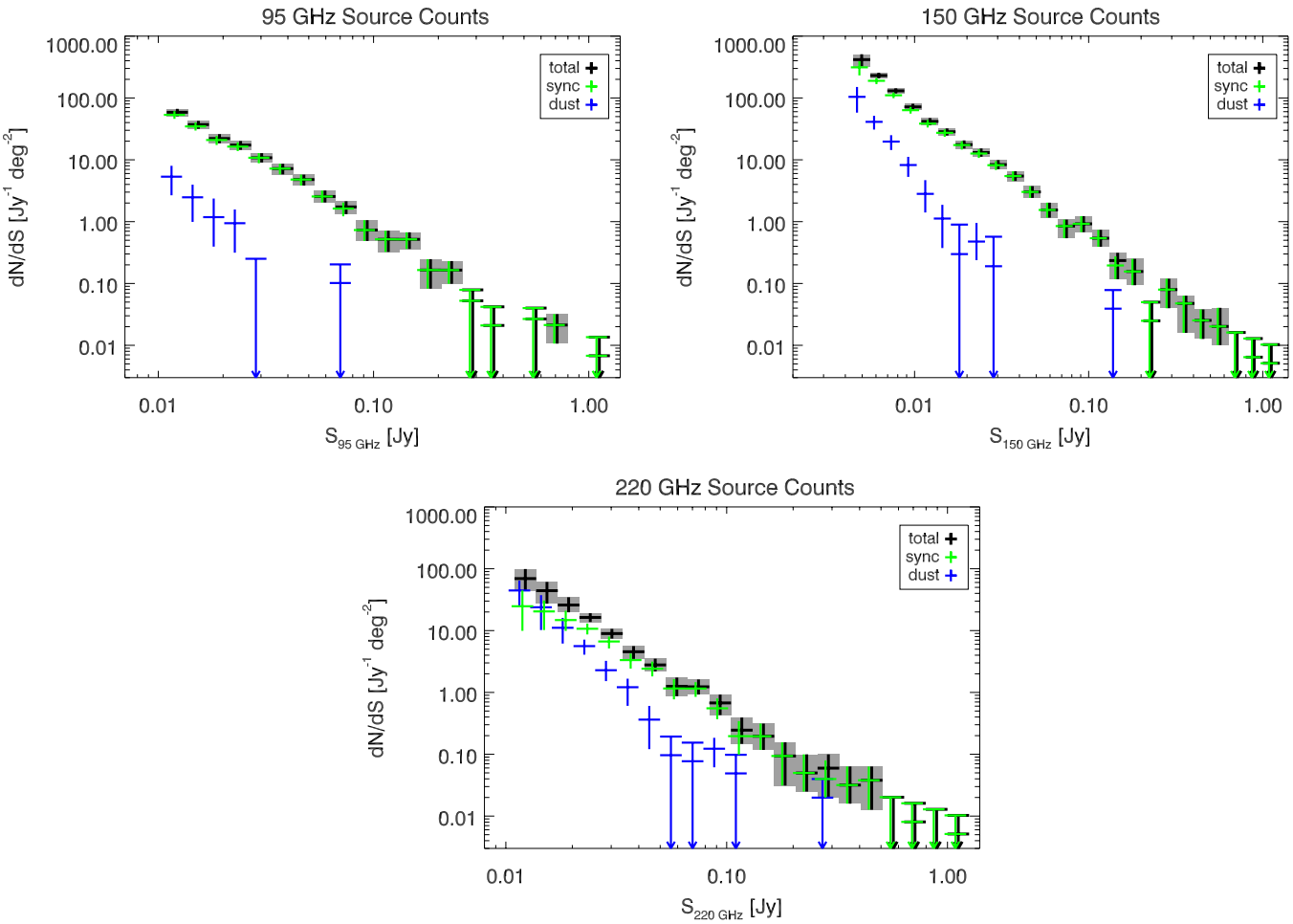

Figure 4. Differential number counts of emissive sources in the three SPT survey bands. Total counts are shown in black, synchrotron-dominated counts are in green, and dust-dominated counts are in blue.

(A color version of this figure is available in the online journal.)

Table 7
The 95 GHz Differential Counts

Flux Density Range (Jy)	dN/dS Total (Jy^{-1} deg^{-2})	dN/dS Sync (Jy^{-1} deg^{-2})	dN/dS Dust (Jy^{-1} deg^{-2})	Completeness
1.1×10^{-2}–1.4×10^{-2}	$(5.87^{+0.8}_{-0.8}) \times 10^{1}$	$(5.33^{+0.8}_{-0.7}) \times 10^{1}$	$5.33^{+2.7}_{-2.7}$	0.93
1.4×10^{-2}–1.7×10^{-2}	$(3.71^{+0.5}_{-0.5}) \times 10^{1}$	$(3.47^{+0.5}_{-0.5}) \times 10^{1}$	$2.48^{+1.5}_{-1.5}$	1.00
1.7×10^{-2}–2.2×10^{-2}	$(2.21^{+0.4}_{-0.4}) \times 10^{1}$	$(2.09^{+0.4}_{-0.4}) \times 10^{1}$	$1.18^{+1.2}_{-0.8}$	1.00
2.2×10^{-2}–2.7×10^{-2}	$(1.73^{+0.3}_{-0.3}) \times 10^{1}$	$(1.64^{+0.3}_{-0.3}) \times 10^{1}$	$(9.44^{+6.3}_{-6.3}) \times 10^{-1}$	1.00
2.7×10^{-2}–3.4×10^{-2}	$(1.08^{+0.2}_{-0.2}) \times 10^{1}$	$(1.08^{+0.2}_{-0.2}) \times 10^{1}$	$0^{+0.3}_{-0}$	1.00
3.4×10^{-2}–4.2×10^{-2}	$7.21^{+1.4}_{-1.4}$	$7.21^{+1.4}_{-1.4}$		1.00
4.2×10^{-2}–5.3×10^{-2}	$4.79^{+1.0}_{-1.0}$	$4.79^{+1.0}_{-1.0}$		1.00
5.3×10^{-2}–6.7×10^{-2}	$2.55^{+0.6}_{-0.5}$	$2.55^{+0.6}_{-0.5}$		1.00
6.7×10^{-2}–8.3×10^{-2}	$1.73^{+0.4}_{-0.4}$	$1.63^{+0.4}_{-0.4}$	$(1.02^{+1.0}_{-1.0}) \times 10^{-1}$	1.00
8.3×10^{-2}–1.0×10^{-1}	$(7.31^{+3.2}_{-2.4}) \times 10^{-1}$	$(7.31^{+3.2}_{-2.4}) \times 10^{-1}$		1.00
1.0×10^{-1}–1.3×10^{-1}	$(5.18^{+1.9}_{-1.9}) \times 10^{-1}$	$(5.18^{+1.9}_{-1.9}) \times 10^{-1}$		1.00
1.3×10^{-1}–1.6×10^{-1}	$(5.17^{+1.6}_{-1.6}) \times 10^{-1}$	$(5.17^{+1.6}_{-1.6}) \times 10^{-1}$		1.00
1.6×10^{-1}–2.1×10^{-1}	$(1.65^{+0.8}_{-0.8}) \times 10^{-1}$	$(1.65^{+0.8}_{-0.8}) \times 10^{-1}$		1.00
2.1×10^{-1}–2.6×10^{-1}	$(1.65^{+0.7}_{-0.7}) \times 10^{-1}$	$(1.65^{+0.7}_{-0.7}) \times 10^{-1}$		1.00
2.6×10^{-1}–3.2×10^{-1}	$(5.25^{+2.6}_{-5.3}) \times 10^{-2}$	$(5.25^{+2.6}_{-5.3}) \times 10^{-2}$		1.00
3.2×10^{-1}–4.1×10^{-1}	$(2.10^{+2.1}_{-2.1}) \times 10^{-2}$	$(2.10^{+2.1}_{-2.1}) \times 10^{-2}$		1.00
5.1×10^{-1}–6.4×10^{-1}	$(2.67^{+1.3}_{-2.7}) \times 10^{-2}$	$(2.67^{+1.3}_{-2.7}) \times 10^{-2}$		1.00
6.4×10^{-1}–8.0×10^{-1}	$(2.13^{+1.1}_{-1.1}) \times 10^{-2}$	$(2.13^{+1.1}_{-1.1}) \times 10^{-2}$		1.00
1.0–1.3	$(6.78^{+6.8}_{-6.8}) \times 10^{-3}$	$(6.78^{+6.8}_{-6.8}) \times 10^{-3}$		1.00

Table 8
The 150 GHz Differential Counts

Flux Density Range (Jy)	dN/dS Total ($\mathrm{Jy}^{-1}\mathrm{deg}^{-2}$)	dN/dS Sync ($\mathrm{Jy}^{-1}\mathrm{deg}^{-2}$)	dN/dS Dust ($\mathrm{Jy}^{-1}\mathrm{deg}^{-2}$)	Completeness
4.4×10^{-3}–5.6×10^{-3}	$(4.17^{+0.9}_{-0.9})\times10^{2}$	$(3.13^{+0.8}_{-0.8})\times10^{2}$	$(1.04^{+0.5}_{-0.5})\times10^{2}$	0.89
5.6×10^{-3}–7.0×10^{-3}	$(2.31^{+0.2}_{-0.2})\times10^{2}$	$(1.89^{+0.2}_{-0.2})\times10^{2}$	$(4.11^{+1.0}_{-1.0})\times10^{1}$	0.85
7.0×10^{-3}–8.7×10^{-3}	$(1.30^{+0.1}_{-0.1})\times10^{2}$	$(1.11^{+0.1}_{-0.1})\times10^{2}$	$(1.97^{+0.5}_{-0.5})\times10^{1}$	0.97
8.7×10^{-3}–1.1×10^{-2}	$(7.17^{+0.9}_{-0.8})\times10^{1}$	$(6.35^{+0.8}_{-0.8})\times10^{1}$	$8.23^{+2.9}_{-2.9}$	1.00
1.1×10^{-2}–1.4×10^{-2}	$(4.17^{+0.6}_{-0.6})\times10^{1}$	$(3.84^{+0.6}_{-0.5})\times10^{1}$	$2.81^{+1.9}_{-1.4}$	1.00
1.4×10^{-2}–1.7×10^{-2}	$(2.84^{+0.4}_{-0.4})\times10^{1}$	$(2.73^{+0.4}_{-0.4})\times10^{1}$	$1.12^{+0.7}_{-0.7}$	1.00
1.7×10^{-2}–2.2×10^{-2}	$(1.76^{+0.3}_{-0.2})\times10^{1}$	$(1.73^{+0.3}_{-0.3})\times10^{1}$	$(2.98^{+6.0}_{-3.0})\times10^{-1}$	1.00
2.2×10^{-2}–2.7×10^{-2}	$(1.31^{+0.2}_{-0.2})\times10^{1}$	$(1.26^{+0.2}_{-0.2})\times10^{1}$	$(4.76^{+4.8}_{-2.4})\times10^{-1}$	1.00
2.7×10^{-2}–3.4×10^{-2}	$8.36^{+1.5}_{-1.3}$	$8.17^{+1.3}_{-1.3}$	$(1.90^{+3.8}_{-1.9})\times10^{-1}$	1.00
3.4×10^{-2}–4.2×10^{-2}	$5.46^{+1.1}_{-0.9}$	$5.46^{+1.1}_{-0.9}$		1.00
4.2×10^{-2}–5.3×10^{-2}	$3.02^{+0.7}_{-0.6}$	$3.02^{+0.7}_{-0.6}$		1.00
5.3×10^{-2}–6.7×10^{-2}	$1.54^{+0.5}_{-0.4}$	$1.54^{+0.5}_{-0.4}$		1.00
6.7×10^{-2}–8.3×10^{-2}	$(8.47^{+2.3}_{-3.1})\times10^{-1}$	$(8.47^{+2.3}_{-3.1})\times10^{-1}$		1.00
8.3×10^{-2}–1.0×10^{-1}	$(9.22^{+3.1}_{-2.5})\times10^{-1}$	$(9.22^{+3.1}_{-2.5})\times10^{-1}$		1.00
1.0×10^{-1}–1.3×10^{-1}	$(5.40^{+2.0}_{-1.5})\times10^{-1}$	$(5.40^{+2.0}_{-1.5})\times10^{-1}$		1.00
1.3×10^{-1}–1.6×10^{-1}	$(2.35^{+0.8}_{-1.2})\times10^{-1}$	$(1.96^{+0.8}_{-0.8})\times10^{-1}$	$(3.91^{+3.9}_{-3.9})\times10^{-2}$	1.00
1.6×10^{-1}–2.1×10^{-1}	$(1.56^{+0.9}_{-0.6})\times10^{-1}$	$(1.56^{+0.9}_{-0.6})\times10^{-1}$		1.00
2.1×10^{-1}–2.6×10^{-1}	$(2.49^{+2.5}_{-2.5})\times10^{-2}$	$(2.49^{+2.5}_{-2.5})\times10^{-2}$		1.00
2.6×10^{-1}–3.2×10^{-1}	$(7.95^{+4.0}_{-4.0})\times10^{-2}$	$(7.95^{+4.0}_{-4.0})\times10^{-2}$		1.00
3.2×10^{-1}–4.1×10^{-1}	$(4.76^{+1.6}_{-3.2})\times10^{-2}$	$(4.76^{+1.6}_{-3.2})\times10^{-2}$		1.00
4.1×10^{-1}–5.1×10^{-1}	$(2.53^{+1.3}_{-1.3})\times10^{-2}$	$(2.53^{+1.3}_{-1.3})\times10^{-2}$		1.00
5.1×10^{-1}–6.4×10^{-1}	$(2.02^{+2.0}_{-1.0})\times10^{-2}$	$(2.02^{+2.0}_{-1.0})\times10^{-2}$		1.00
6.4×10^{-1}–8.0×10^{-1}	$0^{+1.6\times10^{-2}}_{-0}$	$0^{+1.6\times10^{-2}}_{-0}$		1.00
8.0×10^{-1}–1.0	$(6.43^{+6.4}_{-6.4})\times10^{-3}$	$(6.43^{+6.4}_{-6.4})\times10^{-3}$		1.00
1.0–1.3	$(5.13^{+5.1}_{-5.1})\times10^{-3}$	$(5.13^{+5.1}_{-5.1})\times10^{-3}$		1.00

Table 9
The 220 GHz Differential Counts

Flux Density Range (Jy)	dN/dS Total ($\mathrm{Jy}^{-1}\mathrm{deg}^{-2}$)	dN/dS Sync (Jy^{-1} deg^{-2})	dN/dS Dust (Jy^{-1} deg^{-2})	Completeness
1.1×10^{-2}–1.4×10^{-2}	$(6.93^{+3.0}_{-2.5})\times10^{1}$	$(2.48^{+2.0}_{-1.5})\times10^{1}$	$(4.46^{+2.0}_{-2.0})\times10^{1}$	0.84
1.4×10^{-2}–1.7×10^{-2}	$(4.42^{+1.7}_{-1.7})\times10^{1}$	$(2.04^{+1.0}_{-1.0})\times10^{1}$	$(2.38^{+1.4}_{-1.4})\times10^{1}$	0.98
1.7×10^{-2}–2.2×10^{-2}	$(2.59^{+0.9}_{-0.6})\times10^{1}$	$(1.48^{+0.6}_{-0.5})\times10^{1}$	$(1.11^{+0.5}_{-0.5})\times10^{1}$	1.00
2.2×10^{-2}–2.7×10^{-2}	$(1.63^{+0.3}_{-0.3})\times10^{1}$	$(1.07^{+0.2}_{-0.2})\times10^{1}$	$5.61^{+1.5}_{-1.5}$	0.93
2.7×10^{-2}–3.4×10^{-2}	$8.95^{+1.7}_{-1.5}$	$6.67^{+1.3}_{-1.5}$	$2.29^{+1.0}_{-0.8}$	1.00
3.4×10^{-2}–4.2×10^{-2}	$4.55^{+1.1}_{-1.1}$	$3.34^{+0.9}_{-0.9}$	$1.21^{+0.5}_{-0.6}$	1.00
4.2×10^{-2}–5.3×10^{-2}	$2.78^{+0.7}_{-0.6}$	$2.42^{+0.7}_{-0.6}$	$(3.63^{+2.4}_{-2.4})\times10^{-1}$	1.00
5.3×10^{-2}–6.7×10^{-2}	$1.26^{+0.5}_{-0.4}$	$1.16^{+0.5}_{-0.4}$	$(9.65^{+9.7}_{-9.7})\times10^{-2}$	1.00
6.7×10^{-2}–8.3×10^{-2}	$1.23^{+0.4}_{-0.3}$	$1.16^{+0.3}_{-0.3}$	$(7.70^{+7.7}_{-7.7})\times10^{-2}$	1.00
8.3×10^{-2}–1.0×10^{-1}	$(6.76^{+2.5}_{-2.5})\times10^{-1}$	$(5.53^{+2.5}_{-1.8})\times10^{-1}$	$(1.23^{+0.6}_{-0.6})\times10^{-1}$	1.00
1.0×10^{-1}–1.3×10^{-1}	$(2.45^{+1.5}_{-1.0})\times10^{-1}$	$(1.96^{+1.5}_{-1.0})\times10^{-1}$	$(4.90^{+4.9}_{-4.9})\times10^{-2}$	1.00
1.3×10^{-1}–1.6×10^{-1}	$(1.96^{+1.2}_{-0.8})\times10^{-1}$	$(1.96^{+1.2}_{-0.8})\times10^{-1}$		1.00
1.6×10^{-1}–2.1×10^{-1}	$(9.37^{+6.2}_{-6.2})\times10^{-2}$	$(9.37^{+6.2}_{-6.2})\times10^{-2}$		1.00
2.1×10^{-1}–2.6×10^{-1}	$(4.98^{+5.0}_{-2.5})\times10^{-2}$	$(4.98^{+5.0}_{-2.5})\times10^{-2}$		1.00
2.6×10^{-1}–3.2×10^{-1}	$(5.96^{+4.0}_{-4.0})\times10^{-2}$	$(3.98^{+4.0}_{-2.0})\times10^{-2}$	$(1.99^{+2.0}_{-2.0})\times10^{-2}$	1.00
3.2×10^{-1}–4.1×10^{-1}	$(3.17^{+3.2}_{-1.6})\times10^{-2}$	$(3.17^{+3.2}_{-1.6})\times10^{-2}$		1.00
4.1×10^{-1}–5.1×10^{-1}	$(3.80^{+2.5}_{-2.5})\times10^{-2}$	$(3.80^{+2.5}_{-2.5})\times10^{-2}$		1.00
5.1×10^{-1}–6.4×10^{-1}	$0^{+2.0\times10^{-2}}_{-0}$	$0^{+2.0\times10^{-2}}_{-0}$		1.00
6.4×10^{-1}–8.0×10^{-1}	$(8.06^{+8.1}_{-8.1})\times10^{-3}$	$(8.06^{+8.1}_{-8.1})\times10^{-3}$		1.00
8.0×10^{-1}–1.0	$0^{+1.3\times10^{-2}}_{-0}$	$0^{+1.3\times10^{-2}}_{-0}$		1.00
1.0–1.3	$(5.13^{+5.1}_{-5.1})\times10^{-3}$	$(5.13^{+5.1}_{-5.1})\times10^{-3}$		1.00

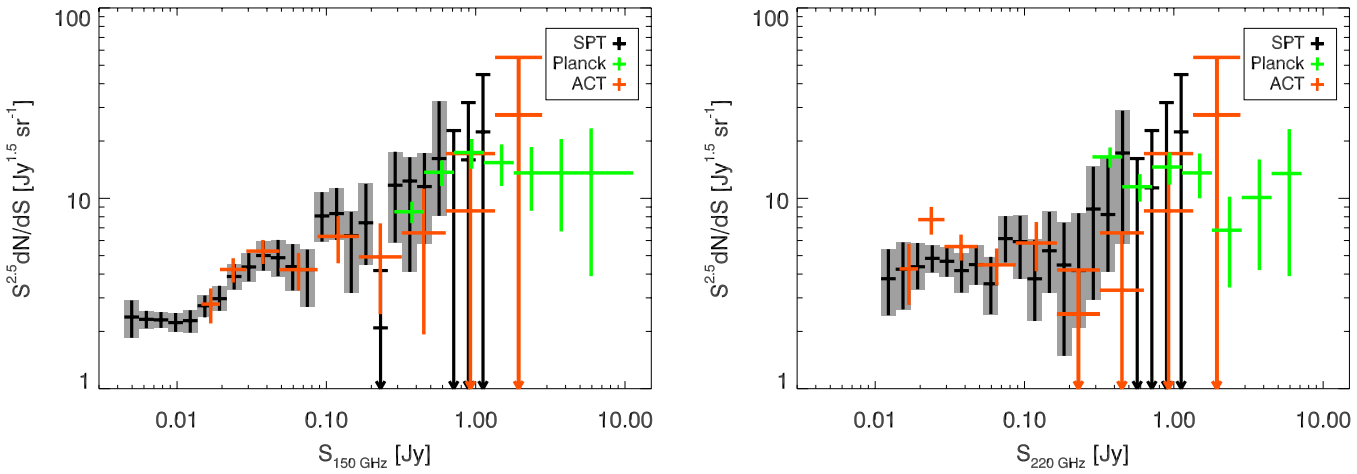

Figure 5. Number counts at 150 and 220 GHz from SPT (this work), Planck (Planck Collaboration et al. 2013a), and ACT (Marsden et al. 2013).
(A color version of this figure is available in the online journal.)

6. DISCUSSION

6.1. Source Populations

In Section 3.6, we classify sources based on their posterior α_{220}^{150} probability distribution. However, given the three observing bands, the picture is inevitably more complicated. Apart from purely falling or rising spectra, we also see spectra that seem to dip or peak within our frequency range. We stress that we define "dipping" and "peaking" sources by the criteria listed in Table 2, such that there might not be an actual trough or peak in the spectrum.

We note that it is possible for sources to scatter out of the standard "falling" and "rising" quadrants into the "peaking" or "dipping" quadrants, especially at low significance. Considering a 7σ detection at 150 GHz (roughly the average significance in the 6–12 mJy column in Table 2), a source with a true $\alpha_{150}^{95} = \alpha_{220}^{150} = -0.7$ gets misclassified as "peaking" 1% of the time, and a source with a true $\alpha_{150}^{95} = \alpha_{220}^{150} = 3.5$ gets misclassified as "dipping" 1% of the time.

The first category ("dipping" sources) comprises what appears to be a synchrotron source at 95 GHz, with dust emission picking up between 150 and 220 GHz. Such sources are expected to be low-redshift ULIRGs or regular spirals. For instance, a source that is spectrally similar to Arp 220, a typical ULIRG (Silva et al. 1998), but had slightly more dust emission would appear in this quadrant of spectral index parameter space. The brightest "dipping" sources are nearby galaxies from the NGC catalog that show both strong radio and starburst activity. Many of these galaxies have counterparts in SUMSS or *IRAS*.

The "peaking" sources are the least numerous population, and the detections are lower S/N, so the spectral indices are more uncertain, but we might see evidence of a self-absorbed synchrotron component in the SED. This is believed to be the emission mechanism in the case of GPS sources (O'Dea 1998), although the subclass with higher turnover frequencies, high-frequency peakers, still typically peaks at tens of GHz (Dallacasa et al. 2000). Most of the brightest such galaxies have radio SUMSS counterparts. Two interesting cases to note are the second and sixth brightest peaking sources, which seem to be associated with the pulsating stars X Pav and NU Pav. About half of the "peaking" sources do not have counterparts in the external catalogs that we have checked.

6.2. Number Counts by Source Population

In this subsection, we will consider models of galaxy number counts from the literature and compare them to the measured counts. We note that, in what follows, we have applied color corrections to all of the models we have considered, to account for small differences between the nominal model bands and our effective instrumental band centers for a typical synchrotron or dusty source, respectively.

6.2.1. Synchrotron-dominated Sources

Figure 6 shows number counts for the synchrotron-dominated population, plotted against the De Zotti et al. (2005) and Tucci et al. (2011) models.

The De Zotti et al. (2005) model takes into account flat- and steep-spectrum radio sources, where the steep-spectrum category includes dusty spheroidals and GPS sources. The model extrapolates blazar spectra using a simple power-law approximation with a spectral index $\alpha \simeq -0.1$ above 100 GHz.

The Tucci et al. (2011) model is constructed based on extrapolations of number counts from high radio frequencies (5 GHz). It considers the spectral behavior of the different source populations, flat-spectrum (FSRQs and BL Lac), steep-spectrum, and inverted spectrum, in a statistical way and takes into account the main physical mechanisms responsible for the emission. The model features different distributions of spectral break frequencies for FSRQs and BL Lacs. We compare our counts to the "C2Ex" version of this model, which was found by the authors to best fit the available high-frequency ($\nu >$ 100 GHz) counts.

Table 10 lists the χ^2 values for the synchrotron-dominated model comparisons. The De Zotti et al. (2005) model fits the lower flux density range rather well and is also a good fit in the intermediate range at 150 GHz, while slightly underpredicting intermediate 95 GHz counts. However, the model is in excess of the data at the high flux density end in all frequency bands. This behavior is most likely due to the simple power-law extrapolation that the model is based on; neglecting the presence of a spectral break leads to overpredicting the number of bright blazars at these frequencies.

The Tucci et al. (2011) model improves upon the former by incorporating the effects of spectral steepening. Consequently, the model is a good fit to our data above 80 mJy and below 20 mJy in all bands, but underpredicts the counts in the

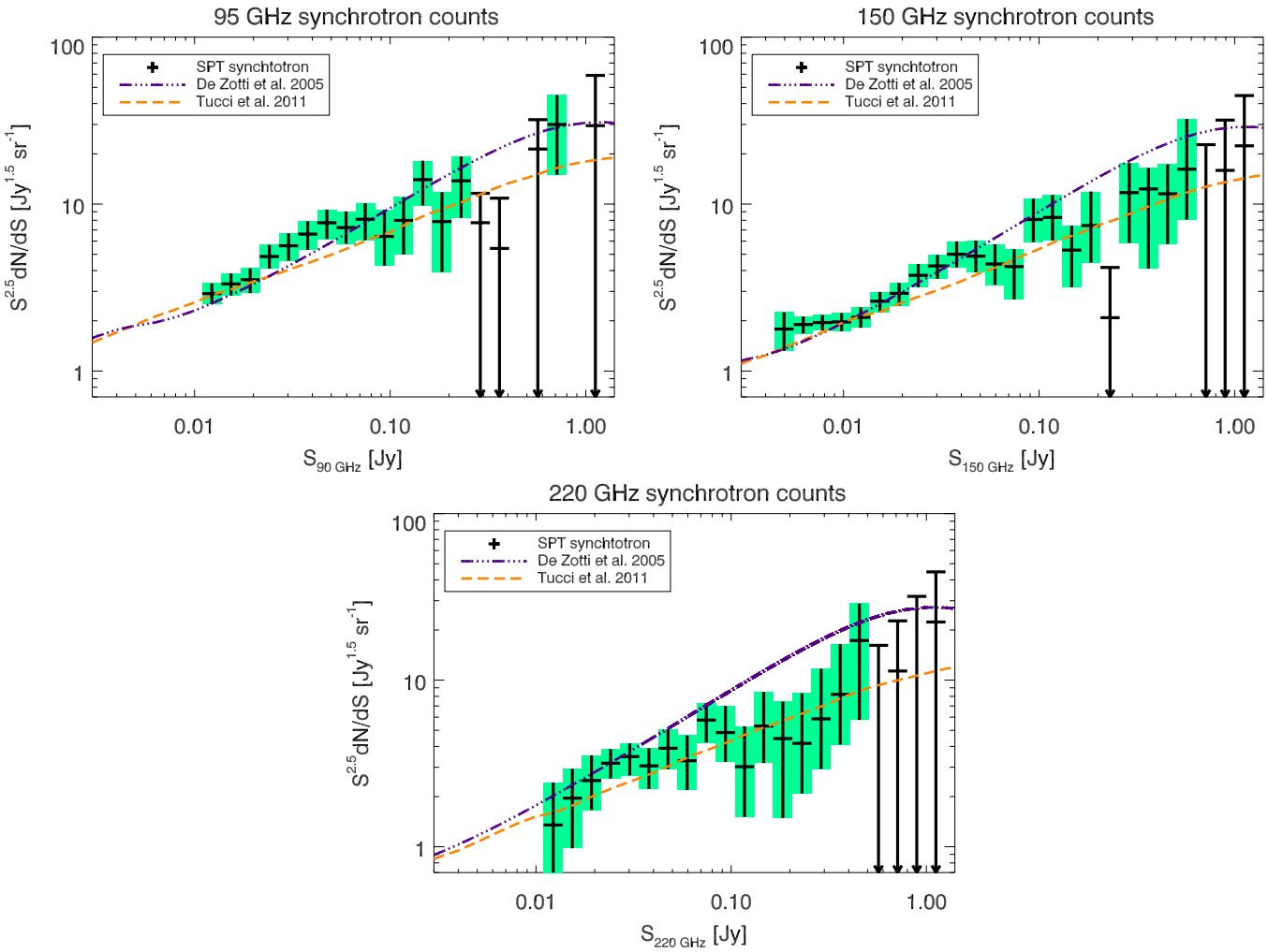

Figure 6. Number counts of SPT synchrotron-dominated sources. Overplotted are the De Zotti et al. (2005) and the Tucci et al. (2011) models. (A color version of this figure is available in the online journal.)

Table 10
AGN Model Goodness of Fit

	95 GHz			150 GHz			220 GHz		
Model	χ^2	dof	PTE	χ^2	dof	PTE	χ^2	dof	PTE
De Zotti et al. (2005)	132.717	21	0	78.671	25	1.834×10^{-7}	86.751	21	0
Tucci et al. (2011)	54.704	21	0	31.386	25	0.177	12.587	21	0.922

Notes. Goodness of fit for the synchrotron number counts models. We list the χ^2 value between the data and the models, the number of degrees of freedom (dof) for the fit, and the probability to exceed (PTE) the χ^2 value.

intermediate flux density range at 95 and 150 GHz. In the 220 GHz band, except for a few bins—again in the tens-of-mJy range—the Tucci et al. (2011) model comes very close to our counts. The discrepancy in all bands in the 10–100 mJy range is possibly an indication that the prescription for spectral steepening as a function of flux level in Tucci et al. (2011) needs to be modified. Specifically, it appears that sources below ∼100 mJy may have a significantly higher break frequency ν_M than is assumed in the Tucci et al. (2011) C2Ex model.

6.2.2. Dust-dominated Sources

Figure 7 shows number counts for dust-dominated sources. Overplotted are the Béthermin et al. (2011), Béthermin et al. (2012), and Cai et al. (2013) models.

The Béthermin et al. (2011) model is a parametric backward evolution model that considers normal and starburst galaxies and is based on an evolution in density and luminosity of the luminosity function, tuned to reproduce a large set of observational constraints—although none of the observational constraints are at SPT observing frequencies. This model includes a strong lensing contribution from high-redshift SMGs.

Béthermin et al. (2012) provide an empirical model based on two star formation modes, corresponding to main-sequence and starburst galaxies. It considers the redshift evolution of these two populations and incorporates two corresponding families of SEDs derived from *Herschel* observations. This model includes the effect of strong lensing on the counts as well, using the lensing prescription of Hezaveh & Holder (2011). All parameters are constrained by non-SPT observations and have not been tuned to fit the SPT counts.

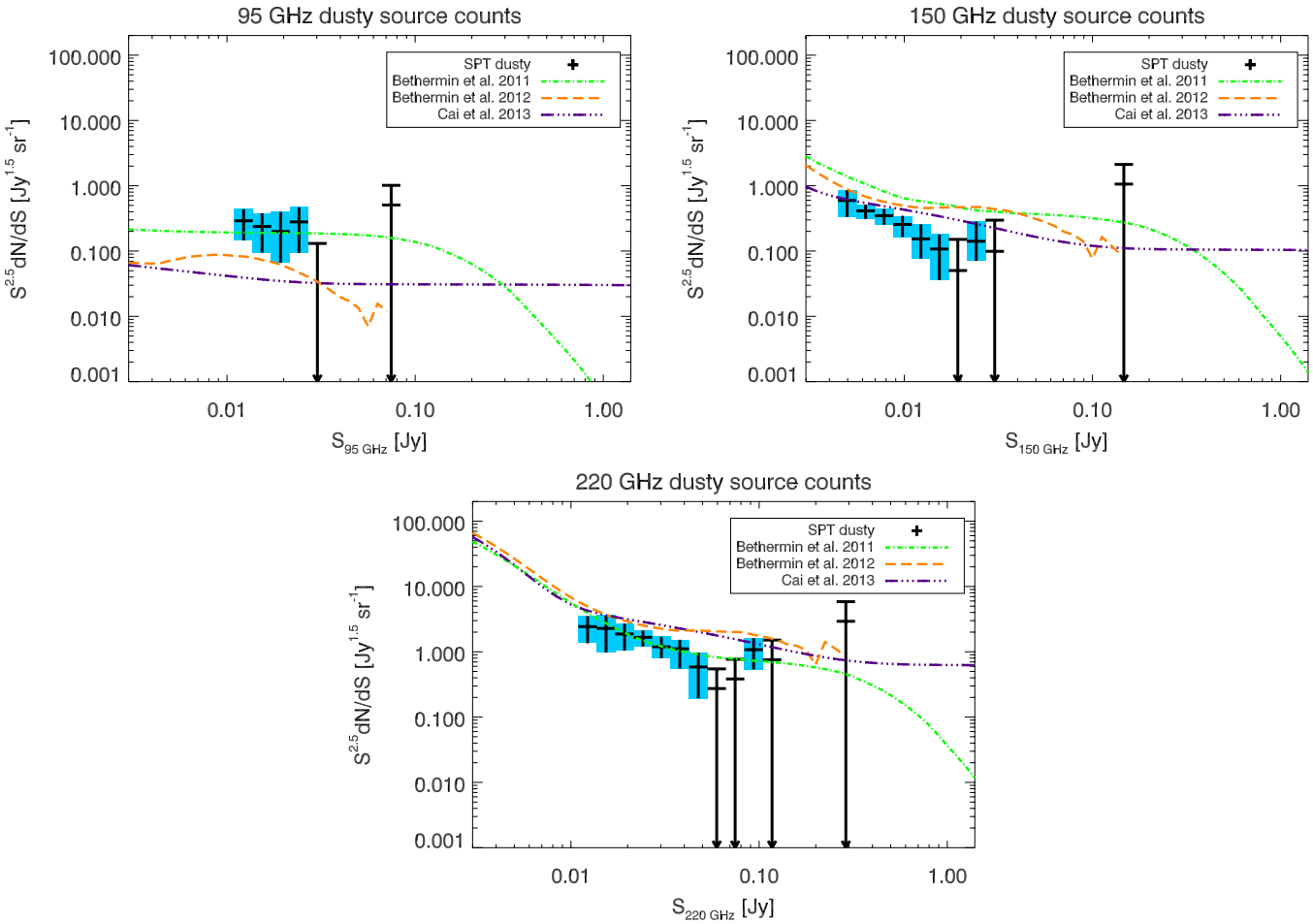

Figure 7. Number counts of SPT dust-dominated sources. Overplotted are the Béthermin et al. (2011), Béthermin et al. (2012), and Cai et al. (2013) models.
(A color version of this figure is available in the online journal.)

Cai et al. (2013) combine a physical forward model for spheroidal galaxies and the early evolution of the associated AGN with a phenomenological backward model for late-type galaxies and for the later AGN evolution. It is calibrated using data from mid-infrared to millimeter wavelengths.

Table 11 lists the χ^2 values for the dusty model comparisons. The Béthermin et al. (2011) model is a very good fit to the data at 95 and 220 GHz, but overpredicts the counts at 150 GHz. It is not clear what causes this behavior.

The Béthermin et al. (2012) model underpredicts the 95 GHz counts, overpredicts the 150 GHz counts above 10 mJy, and overpredicts the 220 GHz counts. This suggests that the model might be assuming too steep a slope for the SED between 95 and 220 GHz. This is plausible since the SED library was calibrated from the far-infrared down to 1.1 mm (∼270 GHz) and extrapolated down to lower frequencies. Slightly warmer local templates would bring down the 150 and 220 GHz counts, while an increase in the synchrotron and/or free–free emission would boost the 95 GHz counts, bringing the model in agreement with the data. The drop in counts at very bright flux density for both the Béthermin et al. (2011) and the Béthermin et al. (2012) models is an artifact of the redshift grid; they should, in fact, converge to a flat behavior.

The Cai et al. (2013) model underpredicts the 95 GHz counts, overpredicts the mid-flux density range 150 GHz counts, and overpredicts the 220 GHz counts.

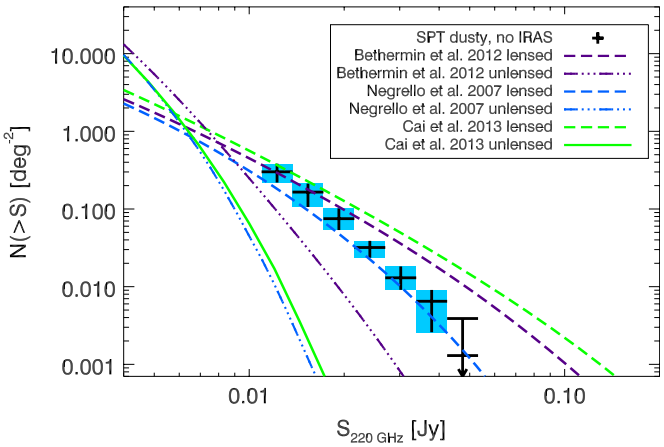

Figure 8. Number counts of SPT dust-dominated sources excluding sources with counterparts in the *IRAS* catalog. Overplotted are the lensed components of the Béthermin et al. (2012), Negrello et al. (2007), and Cai et al. (2013) models.
(A color version of this figure is available in the online journal.)

Figure 8 shows the dust-dominated SPT number counts, excluding sources that have counterparts in the *IRAS* catalog. We overplot the lensed and unlensed components of the Béthermin et al. (2012), Negrello et al. (2007), and Cai et al. (2013) models. To mimic the *IRAS* exclusion, sources with 60 μm flux density

Table 11
Dusty Model Goodness of Fit

	95 GHz			150 GHz			220 GHz		
Model	χ^2	dof	PTE	χ^2	dof	PTE	χ^2	dof	PTE
Béthermin et al. (2011)	3.839	6	0.700	231.192	10	0	7.464	12	0.825
Béthermin et al. (2012)	7.086	6	0.313	123.991	10	0	94.894	12	0
Cai et al. (2013)	9.292	6	0.158	44.765	10	0	81.117	12	0

Notes. Goodness of fit for the dusty number counts models. We list the χ^2 value between the data and the models, the number of degrees of freedom (dof) for the fit, and the probability to exceed (PTE) the χ^2 value.

greater than 200 mJy have been removed from the Negrello et al. (2007) model. We have excluded sources below a redshift of 0.5 from the Béthermin et al. (2012) model and also removed low-redshift populations from the Cai et al. (2013) model.

The counts clearly exceed all the unlensed models and are better fitted by the lensed population models. In particular, the Negrello et al. (2007) model is an excellent fit to the data, suggesting that these counts are well explained by a lensed population of high-redshift dusty sources. The other two models agree at low flux density but overpredict the counts at intermediate to high flux density levels. To correctly predict the lensed counts, a model must make the correct assumptions about both the underlying unlensed population and the lensing magnification probability. It is clear from Figure 8 that the lensed counts in the Béthermin et al. (2012) model are high because the bright tail of the unlensed 220 GHz population is significantly higher than in the other two models, for the reasons discussed above. The unlensed counts in the Cai et al. (2013) model are similar to those in the Negrello et al. (2007) model, indicating that the Cai et al. (2013) prescription for lensing is the cause of the high lensed counts in that model.

Indeed, since the Cai et al. (2013) model was published, the authors have found that the large discrepancy in lensed counts between the Negrello et al. (2007) and the Cai et al. (2013) models is due to the difference in the assumed maximum amplification, $\mu_{\rm max} = 20$ for Negrello et al. (2007) and $\mu_{\rm max} = 100$ for Cai et al. (2013). They found that, by keeping all of the parameters of their model the same and only changing $\mu_{\rm max}$ from 100 to 20, their model is consistent with our data at 150 and 220 GHz. The 95 GHz counts are still underpredicted, which is likely due to an improper combination of free–free and synchrotron emission assumed in their current SED for low-redshift populations, i.e., warm and cold star-forming galaxies (Z. Y. Cai et al. 2013, private communication).

6.2.3. Contamination to CMB Power Spectrum Measurements

The results in this work provide new constraints on the contamination to CMB power spectrum measurements from emissive sources. The source detection threshold in this work (∼5 to ∼10 mJy, depending on observing band) is significantly lower than the detection threshold for Planck (because of the smaller beam and lower per-pixel noise in SPT), and it is also significantly lower than the source threshold used in some SPT power spectrum measurements (K11; Story et al. 2012). The contribution to the power spectrum from sources between these two detection thresholds can serve as a useful constraint in CMB power spectrum analyses.

Assuming a Poisson distribution of point sources, the power spectrum depends on the number counts as

$$C_l = \int_{S_{\rm min}}^{S_{\rm max}} S^2 \frac{dN}{dS} dS. \quad (14)$$

Table 12
Point-source Contamination to Power Spectrum Measurements

ν (GHz)	$S_{\rm min}$ (mJy)	$S_{\rm max}$ (mJy)	$D_{3000}^{\rm total}$ (μK^2)	$D_{3000}^{\rm sync}$ (μK^2)	$D_{3000}^{\rm dust}$ (μK^2)
95	11.0	50	30.70 ± 2.97	29.97 ± 2.98	0.73 ± 0.28
		200	136.67 ± 17.05	134.85 ± 17.05	1.82 ± 0.89
150	4.4	50	8.99 ± 0.68	8.61 ± 0.68	0.38 ± 0.08
		200	32.76 ± 4.53	31.40 ± 4.37	1.37 ± 0.80
220	11.0	50	5.81 ± 0.66	3.81 ± 0.54	2.00 ± 0.39
		200	18.67 ± 2.79	15.59 ± 2.71	3.08 ± 0.60

Notes. D_{3000} values for the Poisson power spectrum contribution of all, AGN, and dusty point sources for each band, between two different flux limits. We note that $D_l = l(l+1)C_l/(2\pi)$.

We evaluate this integral between two flux limits. The lower bound, $S_{\rm min}$, is our lowest flux bin for each band, namely, 11, 4.4, and 11 mJy for 95, 150, and 220 GHz, respectively. We perform the calculation for two different upper bounds. For the first case, we take the threshold $S_{\rm max} = 50$ mJy above which point sources were masked for the CMB power spectrum analysis in Story et al. (2012). For the second case, we use a rough estimate of the point-source cut used in the Planck power spectrum analysis. The actual selection of sources masked in the Planck analysis does not correspond to a clean flux cut in one band (Planck Collaboration et al. 2013b), but a value of 200 mJy at 148 GHz roughly reproduces the Poisson power in the Planck analysis (M. Millea 2013, private communication), so we choose that as our "Planck-like" cut. We summarize the results in Table 12.

6.2.4. Comparison to Source Model Constraints from Fluctuation Measurements

The number counts presented here probe the relatively high flux density end of millimeter-wave source populations, and these results show some difference from published source count models. It is possible to probe to lower flux densities using measurements of the uncorrelated ("Poisson") point-source contribution to the fluctuation power in the same maps that we use here to search for detectable sources. It is reasonable to ask whether measurements of fluctuation power are also different from models, and, if so, whether the discrepancy would be lessened with the same modifications to the models preferred by the source count data. Recent studies of this fluctuation power using SPT data include measurements of the Poisson point-source Fourier-domain two-point function, or power spectrum, in Reichardt et al. (2012) and Fourier-domain three-point function, or bispectrum, in Crawford et al. (2013). Both of these works exclude sources detected above 5σ from the fluctuation analysis, so the results are almost fully independent of the source count results presented here.

We defer a detailed comparison of all three statistics (source counts, power spectrum, bispectrum) and all possible combinations of models to a future work; here we simply note that Crawford et al. (2013), considering a subset of source count models we use in this work, found that no combination of models provided a statistically acceptable fit to the Poisson point-source bispectrum in all three SPT bands. Specifically, the Tucci et al. (2011) model underpredicted the 95 GHz bispectrum (which is expected to be dominated by radio sources), and the Béthermin et al. (2012) model overpredicted the 220 GHz bispectrum (which is expected to be dominated by DSFGs). At 150 GHz, where the radio and DSFG contributions to the bispectrum are both expected to be significant, the Béthermin et al. (2011) and Béthermin et al. (2012) models predict significantly higher bispectrum levels than observed, such that the combined prediction is high regardless of which radio model is used.

If we break the total flux density range probed by bispectrum and source counts into "low-flux" (below the detection threshold used in this work), "moderate-flux" (roughly 10–100 mJy), and "high-flux" (above 100 mJy) regimes, we can draw general conclusions about the radio and DSFG models in the three regimes. We find that the De Zotti et al. (2010) model agrees reasonably well with the data in the low and moderate flux density regimes but overpredicts the counts in the high flux density regime, while the Tucci et al. (2011) model underpredicts the low and moderate flux density counts but accurately predicts the high flux density counts. The DSFG source models considered here and in Crawford et al. (2013) appear to overpredict the 150 GHz counts at all flux density levels. The Béthermin et al. (2011) model accurately predicts the 220 GHz counts in the moderate- and high-flux regimes but overpredicts the low flux density counts, while the Béthermin et al. (2012) model appears to overpredict the 220 GHz counts in all three regimes.

7. CONCLUSION

We have presented a three-band catalog of 1545 sources from 771 deg^2 of the SPT-SZ survey. We have derived deboosted flux densities and spectral indices and have classified the sources into synchrotron- or dust-dominated populations based on their α_{220}^{150} spectral indices.

We have discovered a significant fraction of both synchrotron and dusty sources that have no counterparts in external catalogs. The dusty sources without counterparts represent our lensed SMG candidates: the SPT continues to discover sources that are likely to be high-redshift, strongly lensed SMGs, providing interesting targets to follow up in the submillimeter and other wavebands, particularly with ALMA. The synchrotron-dominated sources with no counterparts could be due simply to source variability, though the number of such sources in this catalog is statistically different from the same number from earlier SPT results based on 87 deg^2 (Vieira et al. 2010). We have also separated sources into four categories based on their position in the two-dimensional spectral index space.

We have derived source number counts in the three SPT frequency bands, including total number counts and number counts for each of the two source populations. Synchrotron sources dominate the number counts everywhere except below 17 mJy in the 220 GHz band. The measured counts can be used to estimate levels of point-source foreground power for CMB analyses from ground-based CMB experiments or the *Planck* satellite.

We have also compared our measured counts to source count models for each population in each frequency band. We find small but significant discrepancies between our measured counts and all the models we consider for either population. The new information provided by our counts thus has the potential to inform models of galaxy formation and evolution as well as models of AGN behavior.

Work is ongoing to extend the analysis presented here to the full 2500 deg^2 SPT-SZ survey. This final catalog will include many new examples of high-redshift, strongly lensed dusty galaxies, and the number counts derived from the full catalog will have smaller uncertainties (by roughly a factor of $\sqrt{3}$), which will lead to improved constraints on models of galaxy formation and evolution, on AGN models, and on the contamination of CMB measurements by point sources.

The SPT is supported by the National Science Foundation through grant ANT-0638937, with partial support provided by NSF grant PHY-1125897, the Kavli Foundation, and the Gordon and Betty Moore Foundation. M. Aravena was co-funded under the Marie Curie Actions of the European Commission (FP7-COFUND). R. Keisler acknowledges support from NASA Hubble Fellowship grant HF-51275.

This publication makes use of data products from the Wide-field Infrared Survey Explorer, which is a joint project of the University of California, Los Angeles, and the Jet Propulsion Laboratory/California Institute of Technology, funded by the National Aeronautics and Space Administration. This research uses observations from the *AKARI* mission, a JAXA project with the participation of ESA. This work is based on observations obtained with Planck (http://www.esa.int/Planck), an ESA science mission with instruments and contributions directly funded by ESA Member States, NASA, and Canada. This research has made use of the NASA/IPAC Extragalactic Database (NED), which is operated by the Jet Propulsion Laboratory, California Institute of Technology, under contract with the National Aeronautics and Space Administration. This research has made use of the SIMBAD database, operated at CDS, Strasbourg, France.

REFERENCES

Aller, M. F., Aller, H. D., & Hughes, P. A. 2011, JApA, 32, 5
Austermann, J. E., Aretxaga, I., Hughes, D. H., et al. 2009, MNRAS, 393, 1573
Austermann, J. E., Aretxaga, I., Hughes, D. H., et al. 2010, MNRAS, 401, 160
Barger, A. J., Cowie, L. L., Sanders, D. B., et al. 1998, Natur, 394, 248
Béthermin, M., Daddi, E., Magdis, G., et al. 2012, ApJL, 757, L23
Béthermin, M., Dole, H., Lagache, G., Le Borgne, D., & Penin, A. 2011, A&A, 529, A4
Blain, A. W. 1996, MNRAS, 283, 1340
Blain, A. W., Chapman, S. C., Smail, I., & Ivison, R. 2004, ApJ, 611, 725
Blain, A. W., Smail, I., Ivison, R. J., Kneib, J.-P., & Frayer, D. T. 2002, PhR, 369, 111
Cai, Z.-Y., Lapi, A., Xia, J.-Q., et al. 2013, ApJ, 768, 21
Carlstrom, J. E., Ade, P. A. R., Aird, K. A., et al. 2011, PASP, 123, 568
Chapman, S. C., Blain, A. W., Smail, I., & Ivison, R. J. 2005, ApJ, 622, 772
Clements, D. L., Rigby, E., Maddox, S., et al. 2010, A&A, 518, L8
Coppin, K., Halpern, M., Scott, D., Borys, C., & Chapman, S. 2005, MNRAS, 357, 1022
Crawford, T. M., Schaffer, K. K., Bhattacharya, S., et al. 2013, arXiv:1303.3535
Crawford, T. M., Switzer, E. R., Holzapfel, W. L., et al. 2010, ApJ, 718, 513
Dallacasa, D., Stanghellini, C., Centonza, M., & Fanti, R. 2000, A&A, 363, 887
De Zotti, G., Massardi, M., Negrello, M., & Wall, J. 2010, A&ARv, 18, 1
De Zotti, G., Ricci, R., Mesa, D., et al. 2005, A&A, 431, 893
Dole, H., Lagache, G., Puget, J.-L., et al. 2006, A&A, 451, 417
Dwek, E., & Arendt, R. G. 1998, ApJL, 508, L9
Engel, H., Tacconi, L. J., Davies, R. I., et al. 2010, ApJ, 724, 233
Foley, R. J., Andersson, K., Bazin, G., et al. 2011, ApJ, 731, 86
Gall, C., Hjorth, J., & Andersen, A. C. 2011, A&ARv, 19, 43

González-Nuevo, J., de Zotti, G., Andreani, P., et al. 2010, A&A, 518, L38
Greve, T. R., Ivison, R. J., Bertoldi, F., et al. 2004, MNRAS, 354, 779
Greve, T. R., Vieira, J. D., Weiß, A., et al. 2012, ApJ, 756, 101
Hainline, L. J., Blain, A. W., Smail, I., et al. 2011, ApJ, 740, 96
Hezaveh, Y. D., & Holder, G. P. 2011, ApJ, 734, 52
Hezaveh, Y. D., Marrone, D. P., Fassnacht, C. D., et al. 2013, ApJ, 767, 132
Högbom, J. A. 1974, A&AS, 15, 417
Hughes, D. H., Serjeant, S., Dunlop, J., et al. 1998, Natur, 394, 241
Ishihara, D., Onaka, T., Kataza, H., et al. 2010, A&A, 514, A1
Ivison, R. J., Greve, T. R., Dunlop, J. S., et al. 2007, MNRAS, 380, 199
Ivison, R. J., Greve, T. R., Smail, I., et al. 2002, MNRAS, 337, 1
Keisler, R., Reichardt, C. L., Aird, K. A., et al. 2011, ApJ, 743, 28
Kovács, A., Chapman, S. C., Dowell, C. D., et al. 2006, ApJ, 650, 592
Lagache, G., Puget, J.-L., & Dole, H. 2005, ARA&A, 43, 727
Larson, D., Dunkley, J., Hinshaw, G., et al. 2011, ApJS, 192, 16
Laurent, G. T., Aguirre, J. E., Glenn, J., et al. 2005, ApJ, 623, 742
Le Floc'h, E., Papovich, C., Dole, H., et al. 2005, ApJ, 632, 169
López-Caniego, M., González-Nuevo, J., Massardi, M., et al. 2013, MNRAS, 430, 1566
Magnelli, B., Saintonge, A., Lutz, D., et al. 2012, A&A, 548, A22
Marsden, D., Gralla, M., Marriage, T. A., et al. 2013, arXiv:1306.2288
Mauch, T., Murphy, T., Buttery, H. J., et al. 2003, MNRAS, 342, 1117
Michałowski, M. J., Dunlop, J. S., Cirasuolo, M., et al. 2012, A&A, 541, A85
Moshir, M., Kopman, G., & Conrow, T. A. O. 1992, IRAS Faint Source Survey, Explanatory Supplement Version 2 (Pasadena: JPL)
Murphy, T., Sadler, E. M., Ekers, R. D., et al. 2010, MNRAS, 402, 2403
Negrello, M., Hopwood, R., De Zotti, G., et al. 2010, Sci, 330, 800
Negrello, M., Perrotta, F., González-Nuevo, J., et al. 2007, MNRAS, 377, 1557
O'Dea, C. P. 1998, PASP, 110, 493
Oliver, S. J., Wang, L., Smith, A. J., et al. 2010, A&A, 518, L21
Planck Collaboration, Ade, P. A. R., Aghanim, N., et al. 2013a, A&A, 550, A133 (Paper VII)
Planck Collaboration, Ade, P. A. R., Aghanim, N., et al. 2013b, arXiv:1303.5075
Planck Collaboration, Ade, P. A. R., Aghanim, N., et al. 2013c, arXiv:1303.5076 (Paper XVI)
Planck Collaboration, Ade, P. A. R., Aghanim, N., et al. 2013d, arXiv:1303.5088 (Paper XXVIII)
Puget, J.-L., Abergel, A., Bernard, J.-P., et al. 1996, A&A, 308, L5
Reichardt, C. L., Shaw, L., Zahn, O., et al. 2012, ApJ, 755, 70
Reichardt, C. L., Stalder, B., Bleem, L. E., et al. 2013, ApJ, 763, 127
Riechers, D. A., Bradford, C. M., Clements, D. L., et al. 2013, Natur, 496, 329
Sanders, D. B., & Mirabel, I. F. 1996, ARA&A, 34, 749
Schaffer, K. K., Crawford, T. M., Aird, K. A., et al. 2011, ApJ, 743, 90
Shirokoff, E., Reichardt, C. L., Shaw, L., et al. 2011, ApJ, 736, 61
Silva, L., Granato, G. L., Bressan, A., & Danese, L. 1998, ApJ, 509, 103
Smail, I., Ivison, R. J., & Blain, A. W. 1997, ApJL, 490, L5
Smolčić, V., Aravena, M., Navarrete, F., et al. 2012, A&A, 548, A4
Soifer, B. T., & Neugebauer, G. 1991, AJ, 101, 354
Stetson, P. B. 1987, PASP, 99, 191
Story, K. T., Reichardt, C. L., Hou, Z., et al. 2012, arXiv:1210.7231
Teerikorpi, P. 2004, A&A, 424, 73
Tegmark, M., & de Oliveira-Costa, A. 1998, ApJL, 500, L83
Tinker, J., Kravtsov, A. V., Klypin, A., et al. 2008, ApJ, 688, 709
Tucci, M., Toffolatti, L., de Zotti, G., & Martínez-González, E. 2011, A&A, 533, A57
Vanderlinde, K., Crawford, T. M., de Haan, T., et al. 2010, ApJ, 722, 1180
Vieira, J. D., Crawford, T. M., Switzer, E. R., et al. 2010, ApJ, 719, 763
Vieira, J. D., Marrone, D. P., Chapman, S. C., et al. 2013, Natur, 495, 344
Voges, W., Aschenbach, B., Boller, T., et al. 1999, A&A, 349, 389
Voges, W., Aschenbach, B., Boller, T., et al. 2000, yCat, 9029, 0
Wardlow, J. L., Cooray, A., De Bernardis, F., et al. 2013, ApJ, 762, 59
Wardlow, J. L., Smail, I., Coppin, K. E. K., et al. 2011, MNRAS, 415, 1479
Weiß, A., De Breuck, C., Marrone, D. P., et al. 2013, ApJ, 767, 88
Wright, A. E., Griffith, M. R., Burke, B. F., & Ekers, R. D. 1994, ApJS, 91, 111
Yamamura, I., Makiuti, S., Ikeda, N., et al. 2010, yCat, 2298, 0